

UC Santa Barbara

UC Santa Barbara Previously Published Works

Title

Investigating spectral distortion of local volcano infrasound by nonlinear propagation at Sakurajima Volcano, Japan

Permalink

<https://escholarship.org/uc/item/4q26b24s>

Journal

J. Geophys. Res. Solid Earth, 125(e2019JB018284)

Authors

Maher, S. P.
Matoza, R. S.
de Groot-Hedlin, C. D.
et al.

Publication Date

2020

DOI

"10.1029/2019JB018284

Peer reviewed

RESEARCH ARTICLE

10.1029/2019JB018284

Investigating Spectral Distortion of Local Volcano Infrasond by Nonlinear Propagation at Sakurajima Volcano, Japan

Key Points:

- Acoustic wavefield simulations suggest significant spectral energy (2 dB) transfer during nonlinear propagation
- Complicated nonlinearity indicator spectra are obtained for observed Sakurajima Volcano infrasond
- Nonlinear signature is modified by spectral contributions from source and propagation complexity

Supporting Information:

- Supporting Information S1

Correspondence to:

Sean P. Maher,
smaher@ucsb.edu

Citation:

Maher, S. P., Matoza, R. S., de Groot-Hedlin, C. D., Gee, K. L., Fee, D., & Yokoo, A. (2020). Investigating spectral distortion of local volcano infrasond by nonlinear propagation at Sakurajima Volcano, Japan. *Journal of Geophysical Research: Solid Earth*, 125, e2019JB018284. <https://doi.org/10.1029/2019JB018284>

Received 1 JUL 2019

Accepted 28 JAN 2020

Accepted article online 5 FEB 2020

Sean P. Maher¹ , Robin S. Matoza¹ , Catherine D. de Groot-Hedlin² , Kent L. Gee³, David Fee⁴ , and Akihiko Yokoo⁵ 

¹Department of Earth Science and Earth Research Institute, University of California, Santa Barbara, CA, USA, ²Scripps Institution of Oceanography, University of California, San Diego, La Jolla, CA, USA, ³Department of Physics and Astronomy, Brigham Young University, Provo, UT, USA, ⁴Wilson Alaska Technical Center, Alaska Volcano Observatory, Geophysical Institute, University of Alaska Fairbanks, Fairbanks, Alaska, USA, ⁵Aso Volcanological Laboratory, Institute for Geothermal Sciences, Graduate School of Science, Kyoto University, Kumamoto, Japan

Abstract Sound waves generated by erupting volcanoes can be used to infer important source dynamics, yet acoustic source-time functions may be distorted during propagation, even at local recording distances (<15 km). The resulting uncertainty in source estimates can be reduced by improving constraints on propagation effects. We aim to quantify potential distortions caused by wave steepening during nonlinear propagation, with the aim of improving the accuracy of volcano-acoustic source predictions. We hypothesize that wave steepening causes spectral energy transfer away from the dominant source frequency. To test this, we apply a previously developed single-point, frequency domain, quadspectral density-based nonlinearity indicator to 30 acoustic signals from Vulcanian explosion events at Sakurajima Volcano, Japan, in an 8-day data set collected by five infrasond stations in 2013 with 2.3- to 6.2-km range. We model these results with a 2-D axisymmetric finite-difference method that includes rigid topography, wind, and nonlinear propagation. Simulation results with flat ground indicate that wave steepening causes up to ~2 dB (1% of source level) of cumulative upward spectral energy transfer for Sakurajima amplitudes. Correction for nonlinear propagation may therefore provide a valuable second-order improvement in accuracy for source parameter estimates. However, simulations with wind and topography introduce variations in the indicator spectra on order of a few decibels. Nonrandom phase relationships generated during propagation or at the source may be misinterpreted as nonlinear spectral energy transfer. The nonlinearity indicator is therefore best suited to small source-receiver distances (e.g., <2 km) and volcanoes with simple sources (e.g., gas-rich strombolian explosions) and topography.

1. Introduction

Volcanic eruptions produce atmospheric sound waves below the 20-Hz frequency threshold of human hearing (infrasond) that can be used to monitor and characterize volcanic activity (e.g., Fee & Matoza, 2013; Garcés et al., 2013; Johnson & Ripepe, 2011; Matoza et al., 2019). Recordings of volcano infrasond at regional (15–250 km) and global (>250 km) distances can be used to detect, locate, and characterize remote eruptions (e.g., Dabrowa et al., 2011; Matoza et al., 2011, 2017, 2019). At these scales, acoustic wavefield distortion by propagation through the dynamic atmosphere is significant and constitutes an active area of research (Assink et al., 2012; Fee et al., 2013; Green et al., 2012; Matoza et al., 2018; Waxler & Assink, 2019). Early work in this field made the assumption that recordings at local distances (<15 km) were directly representative of the source process (e.g., Morrissey & Chouet, 1997); however, it has now been established that near-vent propagation dynamics influence the acoustic wavefield (Fee & Garcés, 2007; Kim & Lees, 2014; Kim et al., 2015; Kim & Lees, 2011; Lacanna & Ripepe, 2013; Matoza et al., 2009). Current work is attempting to develop the capability to use locally recorded volcano infrasond to infer useful eruption source parameters such as gas exit velocity (Matoza et al., 2013; McKee et al., 2016; Woulff & McGetchin, 1976), erupted volume (Firstov & Kravchenko, 1996; Johnson & Miller, 2014; Kim et al., 2015; Yamada et al., 2017), erupted mass (Dalton et al., 2010; Delle Donne et al., 2016; Fee et al., 2017), plume height (Caplan-Auerbach et al., 2010; Lamb et al., 2015; Ripepe et al., 2013), conduit geometry (Buckingham & Garcés, 1996; Garcés, 2000), vent radius (Muramatsu et al., 2018), crater geometry (Johnson, Ruiz, et al., 2018; Johnson, Watson, et al.,

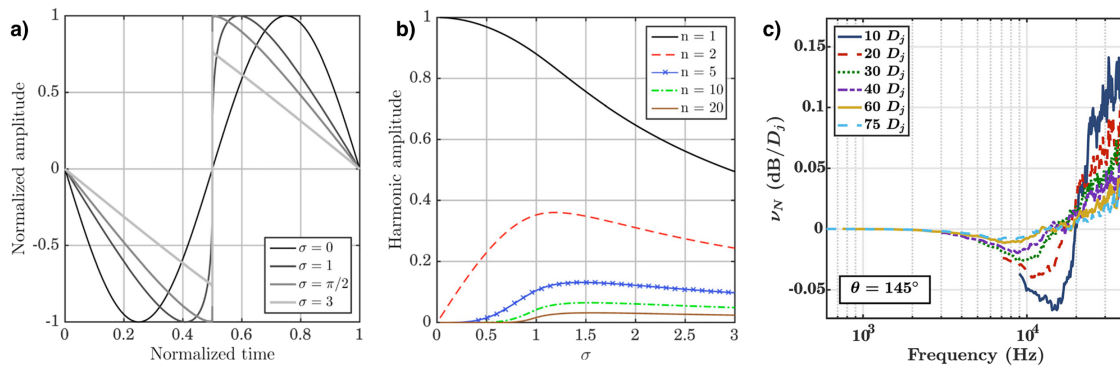


Figure 1. Previously published work by Reichman et al. (2016) and Miller and Gee (2018) illustrating the theory behind the quadrspectral density nonlinearity indicator. (a) Waveform evolution from an initial sinusoid to a shock wave during nonlinear propagation as predicted by the Burgers equation (Reichman et al., 2016). σ represents wavefront propagation distance normalized by shock formation distance. (b) Evolution in amplitude of harmonic frequency components (n) above the fundamental frequency of the initial sinusoid ($n = 1$) as a function of σ (Reichman et al., 2016). Wave steepening during nonlinear propagation causes spectral transfer from the fundamental to higher harmonics. (c) Results of nonlinearity indicator analysis on high-frequency acoustic data from a controlled indoor experiment on model-scale jet noise (Miller & Gee, 2018). The indicator ν_N is here normalized by jet diameter ($D_j = 30$ cm). Each line represents a result from a sensor at a different distance from the jet nozzle along a radial at an angle of $\theta = 145^\circ$ from the jet axis. The reclined S shape of ν_N shows that spectral power is transferred away from the peak source frequency at 10–20 kHz ($\nu_N < 0$) to higher frequencies at which $\nu_N > 0$. Figures are reproduced from Reichman et al. (2016) and Miller and Gee (2018) with permission.

2018; Watson et al., 2019), and source directivity (Jolly et al., 2017; Kim et al., 2012). Therefore, improved understanding of near-source distortions can lead to more accurate estimates of volcano-acoustic source characteristics.

One potential cause of near-source distortion is nonlinear acoustic propagation. While most sound can be accurately modeled by assuming a linear relationship between propagation distance and amplitude decay, this assumption breaks down when amplitudes are large or source processes are supersonic (Atchley, 2005; Garcés et al., 2013; Pierce, 1981). Sound with either of these properties compresses air sufficiently to drive transient adiabatic heating and self-advection that increases the local sound speed (Hamilton & Blackstock, 2008). Consequently, compressional phases travel faster than rarefactional phases such that initially smooth temporal variations in pressure can steepen into shock waves (Figure 1a; Reichman et al., 2016).

Wave steepening causes spectral energy to transfer from the peak source frequency to higher frequencies that are coupled in phase (Kim & Powers, 1979). In the case of an initial sinusoid, these higher frequencies correspond to harmonics on the source frequency (Figure 1b; Reichman et al., 2016). Energy can also be transferred from the peak source frequency to lower frequencies by period lengthening and/or shock coalescence (Hamilton & Blackstock, 2008), although this process is less efficient. Spectral properties estimated from a nonlinearly propagated signal may therefore not reflect properties of the source. For example, analyses of man-made jet noise (Gee et al., 2008; Petitjean et al., 2006) and rocket motor noise (Muhlestein et al., 2012) show that linear acoustic theory underestimates observed power at high frequencies due to upward energy transfer from the spectral peak. Since man-made jet noise exhibits similar characteristics to volcano-acoustic eruption tremor, analogous processes may influence both types of sound (Cerminara et al., 2016; Matoza et al., 2009, 2013; Taddeucci et al., 2014). If nonlinear propagation of volcano infrasound causes energy transfer away from the dominant source frequency, then narrow band-passing filtering around the spectral peak (e.g., Fee et al., 2017; Yamada et al., 2017) may cause underestimation of acoustic source power.

Volcano infrasound has long been thought to propagate nonlinearly near the source (e.g., Garcés et al., 2013; Morrissey & Chouet, 1997), but the distorting effects of this process have not been quantified. Visual observations of wavefronts above erupting vents imply near-source shock wave formation (Ishihara, 1985; Yokoo & Ishihara, 2007), but these waves do not necessarily indicate supersonic sources (Genco et al., 2014). Nonlinear propagation has been proposed as a possible explanation for asymmetric infrasound waveforms, which are commonly observed at volcanoes worldwide (e.g., Anderson et al., 2018; Fee et al., 2013; Marchetti et al., 2013; Matoza et al., 2018; Medici et al., 2013). However, this phenomenon can alternatively be explained with linear propagation and crater rim diffraction (Kim & Lees, 2011) or fluid flow at the source (Brogi et al., 2018). For lack of quantitative understanding of near-source acoustic nonlinearity, volcano-acoustic studies commonly assume linear propagation (e.g., Garcés et al., 2013).

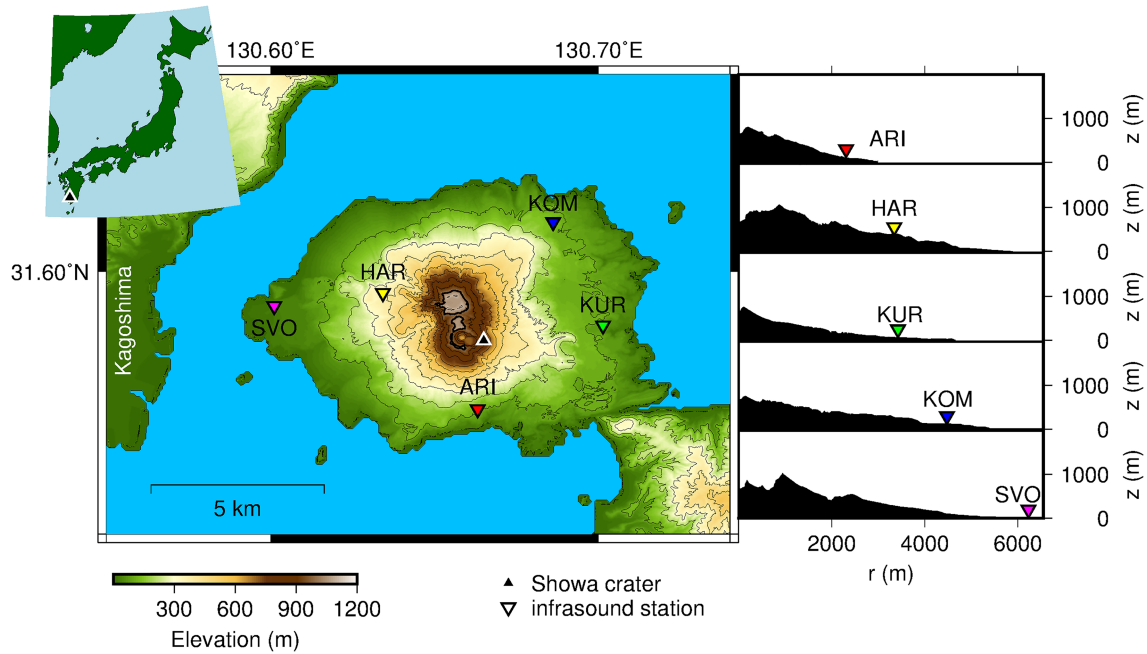


Figure 2. Map of Sakurajima Volcano with 1-m resolution digital elevation model from 2013 showing infrasound station locations (inverted triangles). The active vent in Showa crater (black triangle) is located ~500 m below the dual summits of Kita-Dake (north) and Minami-Dake (south) on the southeast flank of the volcano. Inset map shows the location of Showa crater on Kyushu Island in southern Japan. Profiles at right compare the topography between Showa crater and each station.

In this study we aim to quantify distortions to volcano-acoustic waves by nonlinear propagation using a quadspectral density indicator developed in the high-frequency (audible range 20 Hz to 20 kHz) jet noise literature (Figure 1c; Reichman et al., 2016). We apply the indicator to 30 eruption signals in a 2013 infrasound data set from five sensors at Sakurajima Volcano, Japan (Figure 2). We further apply the method to synthetic pressure data from 2-D axisymmetric cylindrical finite-difference time domain (FDTD) simulations (de Groot-Hedlin, 2016) to investigate the suitability of the indicator and its behavior in the presence of wind and topography. Our study represents the first application of the indicator to infrasound of which we are aware.

1.1. Quantitative Quadspectral Density Nonlinearity Indicator

Various approaches have been used to investigate nonlinear propagation effects such as the statistics of the waveform (e.g., skewness) and its derivative (Anderson et al., 2018; Fee et al., 2013; Gee et al., 2007, 2013), bicoherence (Gee et al., 2007; 2010; Kim & Powers, 1979), and quadspectral density (Gee et al., 2005; Miller et al., 2016; Miller & Gee, 2018; Morfey & Howell, 1981; Petitjean et al., 2006; Reichman et al., 2016). The quadspectral density refers here to the imaginary part of the cross spectrum of pressure and squared pressure (Q_{pp^2}). This spectrum represents phase coupling that arises during summing and differencing of frequency components when energy is transferred to harmonics of the spectral peak (Gagnon, 2011; Kim & Powers, 1979). Quadspectral density potentially provides an appropriate indicator for volcano acoustics since it can reveal quantitative changes in power spectra using single-point measurements.

Following work by Morfey and Howell (1981), Reichman et al. (2016) adapted the frequency domain Generalized Burgers Equation to quantify the spatial rate of change in an acoustic wave's sound pressure level from a single-point measurement. The sound pressure level (unit dB) is $L_p = 10\log_{10}(p_i/p_{ref}^2)$, where p_i is power spectral density (PSD) in an arbitrary frequency band i (unit Pa^2/Hz) and $p_{ref} = 20\mu\text{Pa}/\sqrt{\text{Hz}}$. Reichman et al. (2016) define the rate of change of L_p with respect to source-receiver distance (r) as:

$$\begin{aligned} \frac{\partial L_p}{\partial r} &= -10\log_{10}(e) \times \left(\frac{2m}{r} + 2\alpha + \frac{\omega\beta}{\rho_0 c_0^3} \frac{Q_{pp^2}}{S_{pp}} \right) \\ &\equiv v_S + v_\alpha + v_N \\ &\equiv v, \end{aligned} \quad (1)$$

where $\frac{\partial L_p}{\partial r} = \nu$ is a sum of the effects of frequency-independent geometrical spreading (ν_S), frequency-dependent atmospheric absorption (ν_α), and frequency-dependent nonlinear propagation (ν_N), with unit dB/m. These components can be explicitly defined:

$$\begin{aligned}\nu_S &= -10\log_{10}(e) \times \left(\frac{2m}{r}\right), \\ \nu_\alpha &= -10\log_{10}(e) \times (2\alpha), \\ \nu_N &= -10\log_{10}(e) \times \left(\frac{\omega\beta}{\rho_0 c_0^3} \frac{Q_{pp^2}}{S_{pp}}\right),\end{aligned}\tag{2}$$

where m is a nondimensional geometrical term equal to 0, 0.5, or 1 for planar, cylindrical, or spherical waves, respectively, $\alpha(\omega)$ is the frequency-dependent absorption coefficient of the medium, ω is angular frequency, β is the coefficient of nonlinearity, ρ_0 is ambient density, c_0 is ambient sound speed, and $S_{pp}(\omega)$ is PSD of a pressure time series. The nonlinearity coefficient β is a unitless constant, intrinsic to the medium, which characterizes the effect of finite-amplitude wave propagation on sound speed (Hamilton & Blackstock, 2008). In air, $\beta \approx 1.2$ and can be written as a function of the ratio of specific heats (γ) in an isobaric to an isochoric process, $\beta = \frac{1}{2}(\gamma + 1)$ (Hamilton & Blackstock, 2008). Derivation of equation (1) and further discussion are presented in Appendix A.

Equations (1) and (2) assume that linear spectral changes can be fully described by ν_S and ν_α , neglecting potentially significant effects such as reflections from topography, refraction in temperature gradients, and refraction and advection in wind gradients. Spectral contributions from these processes are inaccurately treated by ν_N as a consequence of nonlinear propagation. The ability of ν_N to accurately describe nonlinear effects consequently depends on the complexity of the signal and recording environment. For example, previous application of a qualitative quadspectral density indicator to outdoor recordings of military jet noise observed evidence for nonlinearity that was modified by interference nulls related to reflections from topography (Gee et al., 2005).

Furthermore, while Equation (1) was developed for analysis of acoustic signals in the audible frequency range, its basis in the Burgers equation dictates that it should be valid for any wave that steepens during propagation due to finite-amplitude effects. Nonlinear steepening of infrasonic waves has previously been postulated at volcanoes (Fee et al., 2013; Lonzaga et al., 2015; Marchetti et al., 2013; Matoza et al., 2019; Morrissey & Chouet, 1997; Yokoo & Ishihara, 2007), so we consider the application of equation (1) to Sakurajima infrasound appropriate.

In this study we focus on the ν_N component of equation (1), since it isolates the effect of nonlinear propagation on the spectrum. Nonlinear acoustic theory predicts that ν_N will express spectral energy transfer as negative values at frequencies where energy is lost and positive values at frequencies where energy is gained. Applications of ν_N to data from indoor experiments on model-scale supersonic jet noise (Miller & Gee, 2018) show that ν_N is negative just above the observed peak frequency and positive at higher frequencies, creating a reclined S shape characteristic of upward spectral energy transfer (Figure 1c). The behavior of ν_N on more complex outdoor signals has not been investigated, and this study represents the first known application to volcano-acoustic data.

1.2. Study Overview

The aim of this study is to investigate the ability of a quadspectral density nonlinearity indicator to quantify distortions to volcano-acoustic signals as a result of nonlinear propagation dynamics. Specifically, we define three hypotheses that are tested throughout this paper:

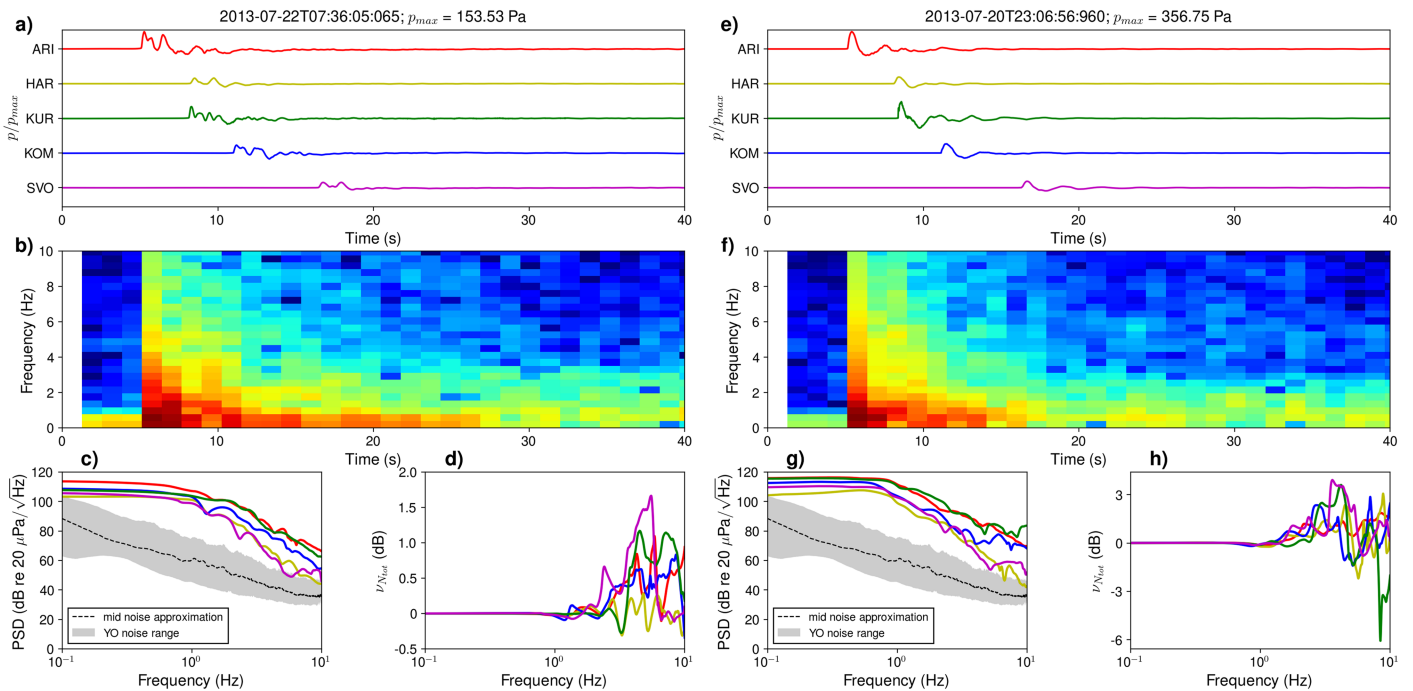


Figure 3. Example of acoustic waveforms, spectra, and nonlinearity indicator results for two eruptions in the Sakurajima 2013 data set. (a) Unfiltered pressure (p) waveforms for a single event arranged in order of increasing vent station distance from top to bottom. Spectral estimation is performed on unfiltered time windows starting 20 s before each station-specific trigger-on time and ending 20 s after the trigger-off time; cropped traces are detrended and multiplied with Tukey windows that taper the first and last 20 s. Signals are normalized by maximum pressure at ARI (p_{max}). (b) Spectrogram showing power spectral density at station ARI for the waveform above. (c) Power spectral density for the waveforms in Figure 3a, compared to the network-averaged noise range in gray. YO is the network code for the 2013 Sakurajima infrasound experiment. (d) Cumulative nonlinearity indicator results ($v_{N_{tot}}$) for the spectra in Figure 3c and waveforms in Figure 3a. The v_N analysis is band limited to 0.1–10 Hz to avoid poor spectral resolution at low frequencies and cultural noise at high frequencies. (e–h) As for parts (a)–(d), but for a higher-amplitude event.

- H1: Nonlinear acoustic propagation of Sakurajima eruption signals causes quantifiable upward spectral energy transfer associated with wave steepening. We test this hypothesis by applying v_N to Sakurajima data (sections 3.1 and 4.4) and to synthetic pressure data from FDTD simulations (sections 3.2, 4.1, and 4.2).
- H2: Acoustic wavefield interactions with topography cause complications in the waveform that obscure the nonlinear signature in v_N . We test this hypothesis by comparing v_N results from nonlinear FDTD modeling with and without topography (sections 3.2 and 4.1).
- H3: Wavefield interactions with wind gradients obscure the nonlinear signature in v_N . We test this hypothesis by comparing v_N results between FDTD simulations with different wind speed gradients (sections 3.2 and 4.2).

2. Sakurajima Volcano and Infrasound Data

Sakurajima Volcano is an active andesitic-dacitic stratovolcano rising 1,117 m above sea level on Kyushu Island in Southern Japan (Figure 2). The volcano's active vent, Showa crater, has produced approximately 1,000 vulcanian-style explosions per year since 2009 (Yokoo et al., 2013). This eruptive activity occurs only ~8 km east of Kagoshima city and poses a constant ash fall hazard to a population of >600,000. Sakurajima is consequently one of the world's best monitored volcanoes (Iguchi et al., 2013), and scientific investigations there have played an important role in explaining Vulcanian eruption processes (e.g., Clarke et al., 2015; Iguchi et al., 2008; Iguchi, 2013; Miwa & Toramaru, 2013; Tameguri et al., 2002; Uhira & Takeo, 1994; Yokoo et al., 2009; 2013).

The data set used in this study features eight days of publicly available acoustic pressure records collected by five infrasound sensors with 200-Hz sample rate at distances of 2.4–6.2 km from Showa crater (Figure 2). The volcano was highly active during the study period (18–26 July 2013) as evidenced by the detection of

34 high-amplitude explosions (Fee et al., 2014) and 74 total explosive events (Matoza et al., 2014). The 74 explosive events identified by Matoza et al. (2014) feature peak pressures of 0.01–449.48 Pa, station-averaged durations of 10–3,000 s, and peak frequencies of 0.4–1 Hz. Typical eruption sequences (e.g., Figures 3a and 3e) feature an initial compression and rarefaction pair corresponding to an explosion (rapid release and expansion of overpressurized gas at the vent), and subsequent lower-amplitude oscillations related to venting of gas and tephra (Fee et al., 2014; Johnson & Miller, 2014) and reflections from topography (Yokoo et al., 2014).

To compare the power spectra of volcanic signals to the background noise range, we estimate the PSD for 50% overlapping 1-hr time windows for the entire data set at each station in the 2013 infrasound deployment. We define network-wide low, median, and high noise conditions as the network-averaged 5th, 50th, and 95th percentiles of the PSD curves, after Bowman et al. (2005) and Brown et al. (2014). Spectra for high-amplitude volcanic signals markedly exceed the 95th percentile in the peak frequency range of approximately 0.4–1 Hz (e.g., Figures 3c and 3g).

3. Methods

3.1. Estimation of Observed v_N

We apply the v_N nonlinearity indicator to 30 acoustic eruption signals with high signal-to-noise ratios out of the 74 events detected by Matoza et al. (2014) using a network-coincident short-term average/long-term average method. We exclude 44 catalog events for which the power spectra of two or more stations fall below the network-averaged median noise condition spectrum in the 0.1- to 10-Hz frequency band (dashed gray line in Figures 3c and 3g). This approach mitigates the contamination of nonlinearity indicator results by wind and/or cultural noise and limits the analysis to higher-amplitude signals for which nonlinear propagation is more likely to be significant (peak pressures of 5.80–449.48 Pa at ARI). These events correspond to impulsive Vulcanian-type eruptions followed by lower-level gas and ash emissions, but significant variability in waveform character, peak pressures, event intensity, and frequency content (Fee et al., 2013; Matoza et al., 2014) suggests that the source process varies between events in terms of vent opening dynamics, volume flux rates (e.g., Johnson and Miller, 2014), and gas/ash ratio.

We estimate PSD and cross-spectral densities of unfiltered waveforms and their squares using a sine multitaper method (Riedel & Sidorenko, 1995). Time windows are defined by the station-specific start and end times of the catalog plus 20 s of Tukey-tapered noise on either side. The addition of 40 s of data increases the frequency resolution of the spectra, while Tukey-tapering preserves the amplitudes of the volcano-acoustic signals and eliminates pressure discontinuities at the window edges.

Nonlinearity indicator results are integrated with respect to station slant distance (i.e., line-of-sight distance) to estimate cumulative spectral changes ($v_{N_{tot}}$), as discussed in Appendix A. Integration assumes a constant rate of spectral change, when in fact the rate of change decreases with decaying signal amplitude (Miller & Gee, 2018). Since Sakurajima stations are several kilometers from the source, observed v_N likely represents a smaller rate of change than what occurs near the source. Cumulative $v_{N_{tot}}$ therefore likely underestimates the total spectral changes; however, we present integrated results rather than raw v_N because they are more applicable to a spectral correction scheme and because they are easier to compare to other distorting processes such as geometrical spreading.

To facilitate comparison of v_N across all events we extract several metrics from $v_{N_{tot}}$ and associated signals (Figure 10) including the following:

- Centroid frequency, $f_c = \frac{\int_{f_1}^{f_2} f S_{pp} df}{\int_{f_1}^{f_2} S_{pp} df}$, where f_1 and f_2 are the high- and low-frequency bounds of interest, f is the bounded frequency range, and S_{pp} is power spectral density (Johnson, 2019). Use of f_c is preferable to peak frequency in this case because the spectral peaks are broad at low frequencies (e.g., Figures 3c and 3g).
- PSD and $v_{N_{tot}}$ at f_c .
- Maximum and minimum $v_{N_{tot}}$ and associated frequencies.
- Maximum signal pressure.

Since wave steepening causes energy to transfer primarily to frequency components higher than the dominant source frequency, we expect to see $v_N < 0$ (energy loss) at f_c and $v_N > 0$ (energy gain) at $f > f_c$. We

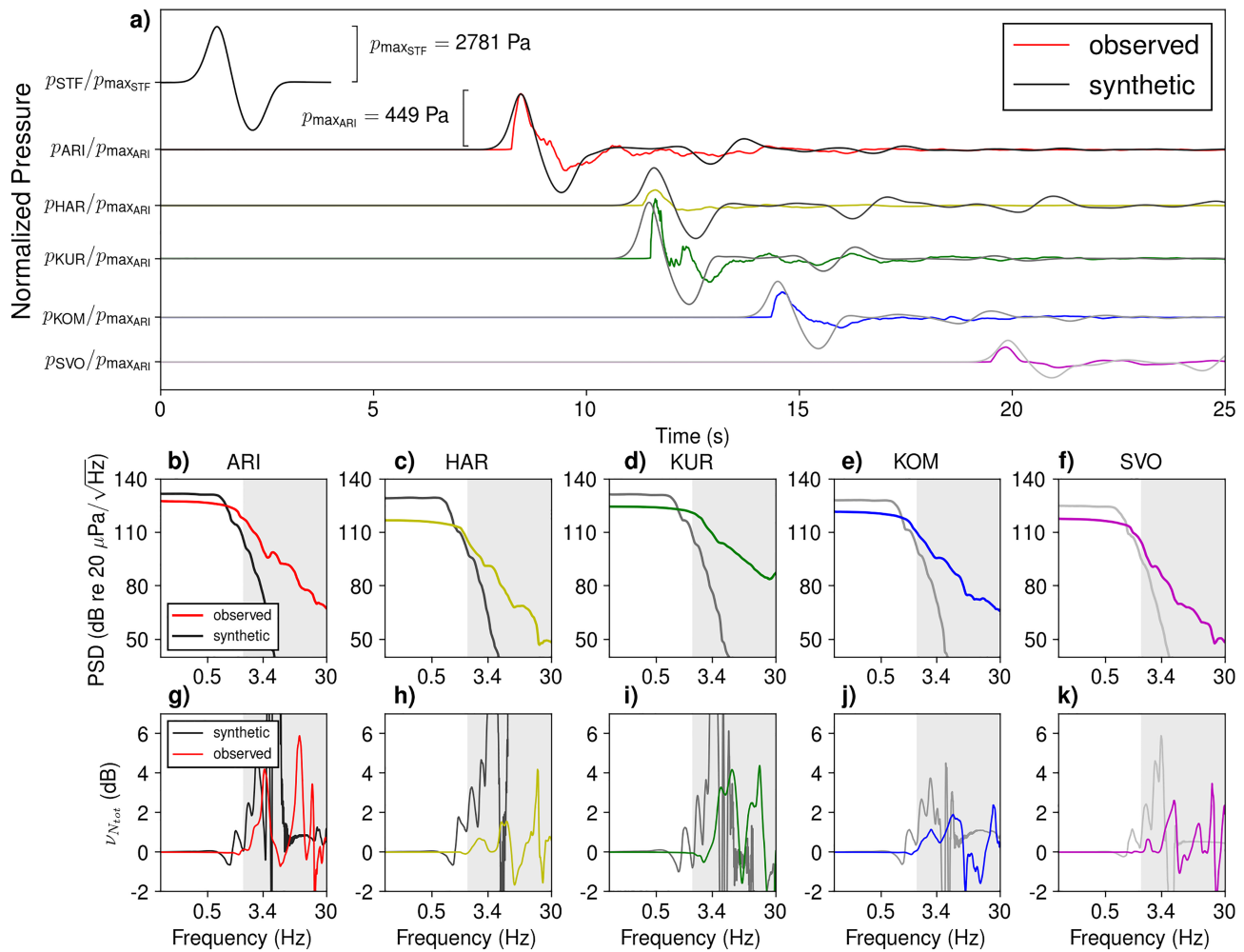


Figure 4. Comparison of synthetic data from windless nonlinear Simulation Set S1 (solid grayscale lines) with observational data from a Sakurajima eruptive event at 23:21:49 UTC on 20 July 2013 (colored lines). (a) Waveform comparison. The first trace shows the approximate source-time function (\sim STF) as recorded by a synthetic receiver at one grid cell from the left boundary at the top of the source function (8.5 m range, 1,274 m altitude). The five trace pairs below show observed and synthetic waveforms that are time aligned by the time of peak pressure at real and synthetic ARI stations. Amplitudes of the STF are normalized by the peak pressure of the STF ($p_{\max\text{STF}}$), while the other waveforms are normalized by the peak pressure at the real ARI station ($p_{\max\text{ARI}}$). (b–f) Power spectral densities for the waveforms in Figure 4a plotted by station. For each trace, the PSD is estimated on 31-s windows (7 s before and 24 s after peak pressure) that are detrended and tapered with a 20% Tukey window. (g–k) Cumulative v_N estimates for the spectra in Figures 4b–4f. Note that synthetic frequency components are most accurate below 1.7 Hz, whereas the observed spectra are have power over a broader frequency range. The gray shaded region indicates frequency components above 1.7 Hz for which synthetic spectra may be inaccurate due to numerical dispersion.

expect this to be expressed as a positive correlation between f of minimum $v_{N_{\text{tot}}}$ and f of maximum $v_{N_{\text{tot}}}$, and negative values of $v_{N_{\text{tot}}}$ at f_c . Furthermore, since higher pressures gives rise to greater phase speeds (Hamilton & Blackstock, 2008), we expect a positive correlation between maximum signal pressure and maximum $v_{N_{\text{tot}}}$ and a negative correlation between maximum signal pressure and minimum $v_{N_{\text{tot}}}$. These relationships have been qualitatively observed in applications to computationally propagated waves (Reichman et al., 2016; Miller et al., 2016) and model-scale jet noise (Miller & Gee, 2018), as shown in Figure 1c. This study is the first to extract quantitative metrics from v_N .

3.2. Nonlinear FDTD Modeling of v_N

We model the acoustic wavefield at Sakurajima with a FDTD method for nonlinear infrasound propagation developed by de Groot-Hedlin (2017). The method includes rigid stair-step topography at the lower boundary, vertical 1-D gradients in sound and wind speeds, and spherical spreading in a 2-D model plane by implementation of a cylindrical coordinate system that is axisymmetric about the left boundary. The model is bounded at the top and right by absorbing Perfectly Matched Layers (Berenger, 1994) set at a maximum range and height of 15 km. This choice ensures that any potential artificial reflections from the top and right

Table 1
Summary of Input and Discretization Parameters for FDTD Modeling

S _{ID}	LB	SA (Pa)	Wind	Δt (ms)	Δ (m)	NDX	H _{ID}
S1	both	47,500	no	7.4	9.0	20	H1
S2	topo	47,500	toward ARI	7.0–7.6	8.5–9.5	20	H1
S3	topo	47,500	toward HAR	7.0–7.6	8.5–9.5	20	H3
S4	topo	47,500	toward KOM	7.0–7.6	8.5–9.5	20	H3
S5	topo	47,500	toward KUR	7.0–7.6	8.5–9.5	20	H3
S6	topo	47,500	toward SVO	7.0–7.6	8.5–9.5	20	H3
S7	flat	47,500	toward all	7.6	9.5	20	H3
S8	flat	47,500	away from all	6.9	8.4	20	H3
S9	both	47,500	no	3.7	4.5	40	H1
S10	flat	1,484–95,000	no	7.4	9.0	20	H1

Note. S_{ID} is simulation set identification label, LB is lower boundary type (flat, topography, or both), SA is source amplitude, Δt is time step, Δ is grid spacing, NDX is number of grid cells required per wavelength at the maximum source frequency and minimum sound speed, and H_{ID} is hypothesis identification number in reference to section 1.2. H_{ID} indicates which hypothesis the simulation set is mainly intended to address. Simulations Sets S1–S9 with topography include five simulations (one for each source-receiver profile) while those with flat ground feature one simulation with all receivers on the same profile. S10 includes eight simulations with different SA values.

boundaries do not reach the synthetic receivers (maximum range of 6.2 km) before the end of the simulation at 44 s. We use a linear sound speed gradient of 6°K/km from 348 m/s at sea level to 308 m/s at 11 km and constant above this.

At the start of each simulation the source function is initialized as a spatially distributed Gaussian pulse of positive pressure with radius equal to three times the maximum source wavelength at the sound speed of the source altitude. The pulse is truncated at the source radius such that the pressures and densities in the rest of the model space are initialized to ambient values. Rapid wavefield changes during high-amplitude propagation can lead to numerical instability (de Groot-Hedlin, 2017), so we use flat topography within the source radius to avoid initializing complex interference patterns from reflections inside the crater (e.g., Figure 6). We approximate the source-time function (STF) by placing a synthetic receiver one grid cell from the left boundary and one grid cell above the top of the source radius and cropping the waveform before the arrival of the ground reflection. This yields a waveform with a nearly symmetrical compression-rarefaction pair (Figure 4a). This source implementation produces peak frequencies of approximately one third the maximum input source frequency (f_{\max}) for linear propagation modeling; for the nonlinear modeling used here, spectral energy transfer may lead to lower peak frequencies.

We test the hypotheses presented in section 1.2 by systematically varying the simulation inputs. Table 1 summarizes the input and discretization parameters for the 10 simulation sets presented here (47 total simulations). Notably, the time step (Δt) and grid spacing (Δ) vary by simulation to meet the Courant stability criterion as a function of the maximum source frequency, maximum source pressure, and minimum number of grid nodes (NDX) per wavelength at f_{\max} . The Courant stability criterion (Taflove & Hagness, 2005) is $\Delta t \leq \Delta / c_{\max} \sqrt{3}$, where c_{\max} is the maximum sound speed. At least 10 grid nodes per wavelength are required at c_{\max} to maintain numerical accuracy (Taflove & Hagness, 2005). In this study we require 20 NDX at a maximum source frequency of $f_{\max} = 1.7$ Hz in each simulation; this means that the 10 NDX criterion for stability is met for frequencies up to 3.4 Hz and 60 to 80 nodes per wavelength are present at the dominant frequency range below ~0.8 Hz.

To test the accuracy of the frequency components, we separately ran a nonlinear simulation set with NDX = 40 at 1.7 Hz (Set S9). Increased discretization does not affect the shapes or amplitudes of the power spectra or v_N spectra at frequency components $f < 1.7$ Hz, but it does result in small increases in PSD and v_N values with frequency above 1.7 Hz (Figures S1 and S2 in the supporting information). From this we conclude that inaccuracies arising from numerical dispersion are negligible at frequencies less than 1.7 Hz but may impact results at higher frequencies. We therefore only interpret synthetic results at frequencies below

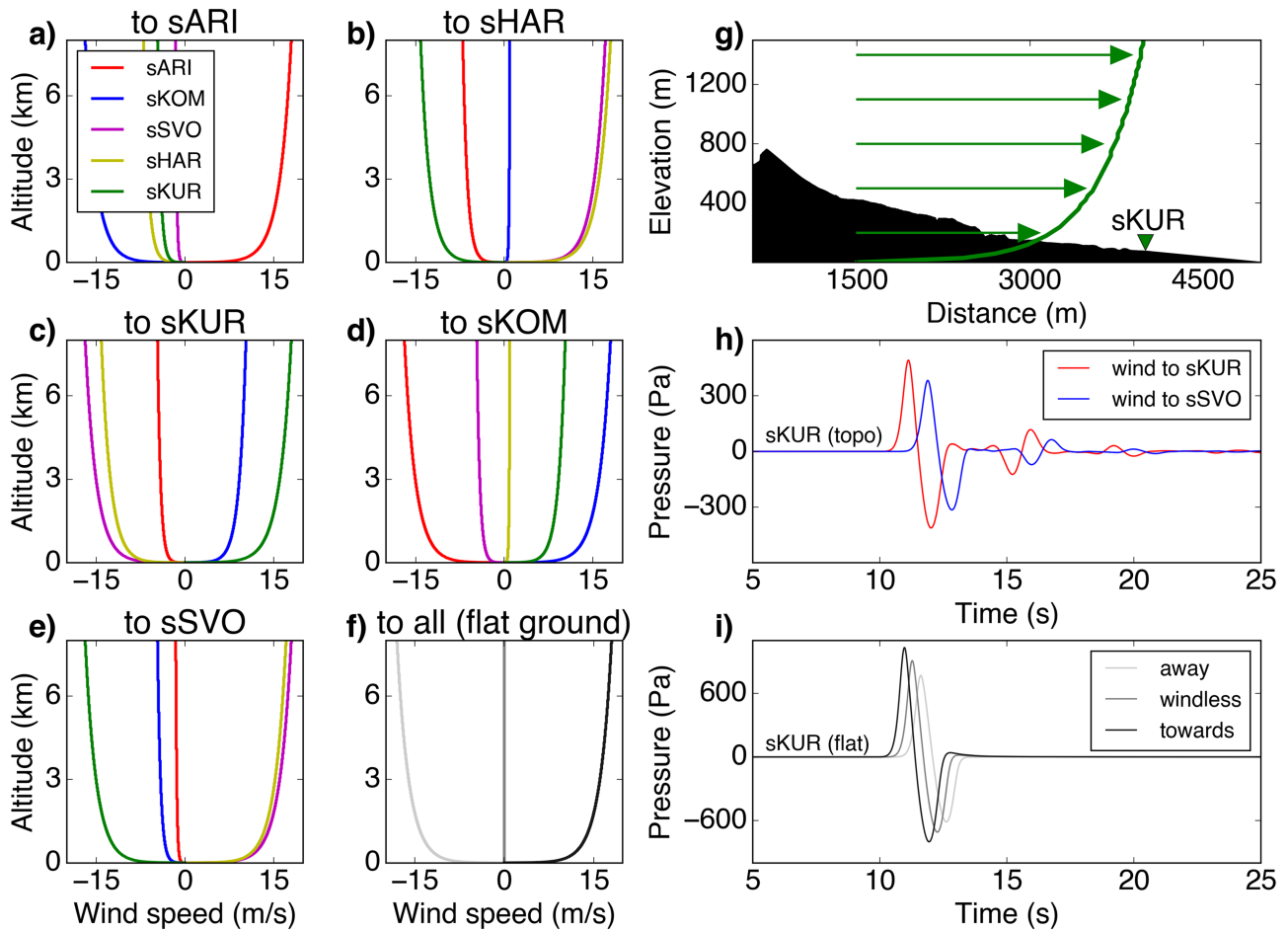


Figure 5. (a–e) Logarithmic wind profiles for nonlinear FDTD Simulations S2–S8 (Table 1). The maximum wind speed profile is directed toward the station in the subplot title, and wind profiles at other stations are rotated by the azimuth difference. (f) Logarithmic wind profiles for the flat ground simulations including the windless condition (S1) and conditions for which wind is directed toward all stations (S7) or away (S8). (g) Topographic profile for station sKUR (triangle) illustrating the wind condition for a wind speed vector directed towards the station (not to scale). Arrows show how wind speed increases with height. Vertical exaggeration is approximately 2:1. (h) Waveforms at station sKUR for simulations with topography in which wind is blowing towards sKUR (red) and toward sSVO (blue). (i) Waveforms at station sKUR for flat ground stations with windless condition and with wind blowing toward and away from the station. Compared to downwind propagation, upwind propagation results in a delayed travel times and reduced amplitudes.

1.7 Hz. In this manuscript we show synthetic results up to 3.4 Hz but indicate frequencies greater than 1.7 Hz with grey shaded boxes.

We run simulations over 2-D topography profiles (Figure 2) using a 1-m resolution digital elevation model (DEM) to model v_N results in the Sakurajima data set. We use a 10-m resolution DEM covering a large area over Kagoshima Bay and a smaller 1-m resolution DEM covering Showa crater and the summit region of Sakurajima. The 10-m resolution DEM is interpolated to 1-m resolution using a bivariate spline approximation over a rectangular mesh and fused with the true 1-m resolution DEM. The 1-m resolution stair steps are discretized to the 8.5- to 9.5-m grid spacing in the model space, but these larger steps are sufficiently small relative to the shortest wavelength of interest in the simulations (~ 100 m for 3.4 Hz at 340 m/s) to minimize the magnitude of artificial reflections. Small artificial reflections similar to diffraction grating (constructive interference between waves reflected from different stair-step faces) are possible even with very small steps (e.g., de Groot-Hedlin, 2004); however, the magnitude of these are small compared to the specular reflections.

We choose $f_{\max} = 1.7$ Hz to match the approximate spectral peak of the Sakurajima signals (0.4–1 Hz), and a source overpressure of 47,500 Pa to match amplitudes at the closest station to that of the largest event in the data set (449 Pa at 2.3 km). We use a nonlinear-linear transition threshold of 0.3% ambient pressure

(transition at ~ 304 Pa) after de Groot-Hedlin (2017). To test the influence of topography on v_N , we compare these results to simulations run over flat ground (S1).

To test the influence of wind, we run five sets of simulations in which a wind speed profile of $w_0 = 2\log_{10}(z)$ is directed toward one station and rotated for the other stations by $w_n = w_0 \cos(\theta)$, where θ is the azimuth difference between two stations (Figures 5a–5e). We bracket the parameter space for the flat ground simulations by directing wind over flat ground toward and away from all the stations (Figure 5f). The wind profiles, following work by Jones et al. (1986), are not intended to simulate local meteorological conditions during the field deployment but rather to test the influence of wind on v_N under maximum likely wind conditions.

Finally, we test the response of v_N to variable strengths of nonlinearity by running eight simulations with different maximum input pressures ranging from 1.48 to 95.00 kPa (Simulation Set S10 in Table 1). We approximate free-field propagation by setting the source and receiver altitudes at 7.5 km above a flat lower boundary at sea level. Reflected waves from the upper and lower boundaries are avoided by stopping the simulations before the reflected arrivals. We measure changes very close to the source by placing 10 synthetic receivers at 100-m intervals starting 10 m outside the edge of the source radius.

4. Results

4.1. Influence of Topography on Modeled v_N Results

Similar to previous work (Kim & Lees, 2014, 2011; Lacanna & Ripepe, 2013; Lacanna et al., 2014), our FDTD modeling shows that reflections from topography create arrivals that are visible in the wavefield (Figure 6) and as additional waveform arrivals following the source pulse (Figures 7a and 7i) that create irregularities in the associated PSD (Figures 7b and 7j). Propagation over rougher topography induces delayed travel times, amplitude reductions in the waveforms (Figures 7a and 7i), and power reductions in the spectra (Figures 7b, 7c, 7j, and 7k) compared to propagation over flat ground. For example, at the distance of station SVO, nonlinear propagation simulations show that the peak pressure is reduced by 34% and the arrival time is delayed by 0.62 s when topography is included compared to flat ground.

Figure 7 shows that upward spectral energy transfer is modeled when nonlinear propagation equations are used. Power spectra for the results from the flat ground model space (Figure 7c) show a gain in power at frequencies above the spectral peak (1.2–3.4 Hz) compared to the approximate source time function. This energy gain is also visible in the PSDs from simulations with Sakurajima profiles (Figures 7b), but it is distorted by wavefield interactions with topography.

The $v_{N_{tot}}$ results from simulations with flat ground (Figures 7d–7h) show the reclined S-shape indicative of upward spectral energy transfer as expected from previous studies (Miller & Gee, 2018) and shown in Figure 1c. These results show that ≤ 1 dB of spectral energy is transferred away from the 0.8- to 1.2-Hz frequency components primarily to higher frequencies (1.2–3.4 Hz), with up to 6.5 dB gain at 3.4 Hz at synthetic KUR. The spectral energy gains peak at approximately 1.35, 2.05, 2.75, and 3.4 Hz, as estimated from the flat ground sKUR $v_{N_{tot}}$ spectra. These peaks correspond to harmonics on a 0.68-Hz fundamental frequency, but the peak frequency of the source-time function is 0.57 Hz. However, at this distance from the center of the source a small amount of wave steepening by nonlinear propagation occurs, as evidenced by secondary peaks in the source PSD (Figures 7b and 7c) and nonzero $v_{N_{tot}}$ values (Figure 7d). The 0.57-Hz spectral peak may therefore be lower than the 0.68-Hz fundamental because a small amount of energy has transferred away from the peak source frequency. We also note the spectral peak is broad enough to include the 0.68-Hz fundamental (Figures 7b and 7c). Additionally, at the synthetic stations at Sakurajima distances, a small amount of power is also transferred downward by period lengthening (~ 0.1 dB between 0.4 and 0.8 Hz). Inclusion of Sakurajima topography reduces $|v_{N_{tot}}|$ levels and complicates the $v_{N_{tot}}$ spectral shapes (Figures 7d–7h). However, the effect of topography is not sufficient to explain the complexity in the $v_{N_{tot}}$ results from the observed Sakurajima signals as shown in Figures 4g–4k and discussed in section 4.4.

4.2. Influence of Wind on Modeled v_N Results

Since wavefield interactions with topography are insufficient to explain the complexity of the observed Sakurajima v_N spectra (see Figures 4g–4k), we investigate the effect of wind on the ability to observe nonlinear effects. Upwind propagation results in delayed arrival times and reduced amplitudes in the waveform (Figures 5h and 5i) and frequency-independent reductions in the PSD (Figures 8a–8e). Conversely, upwind

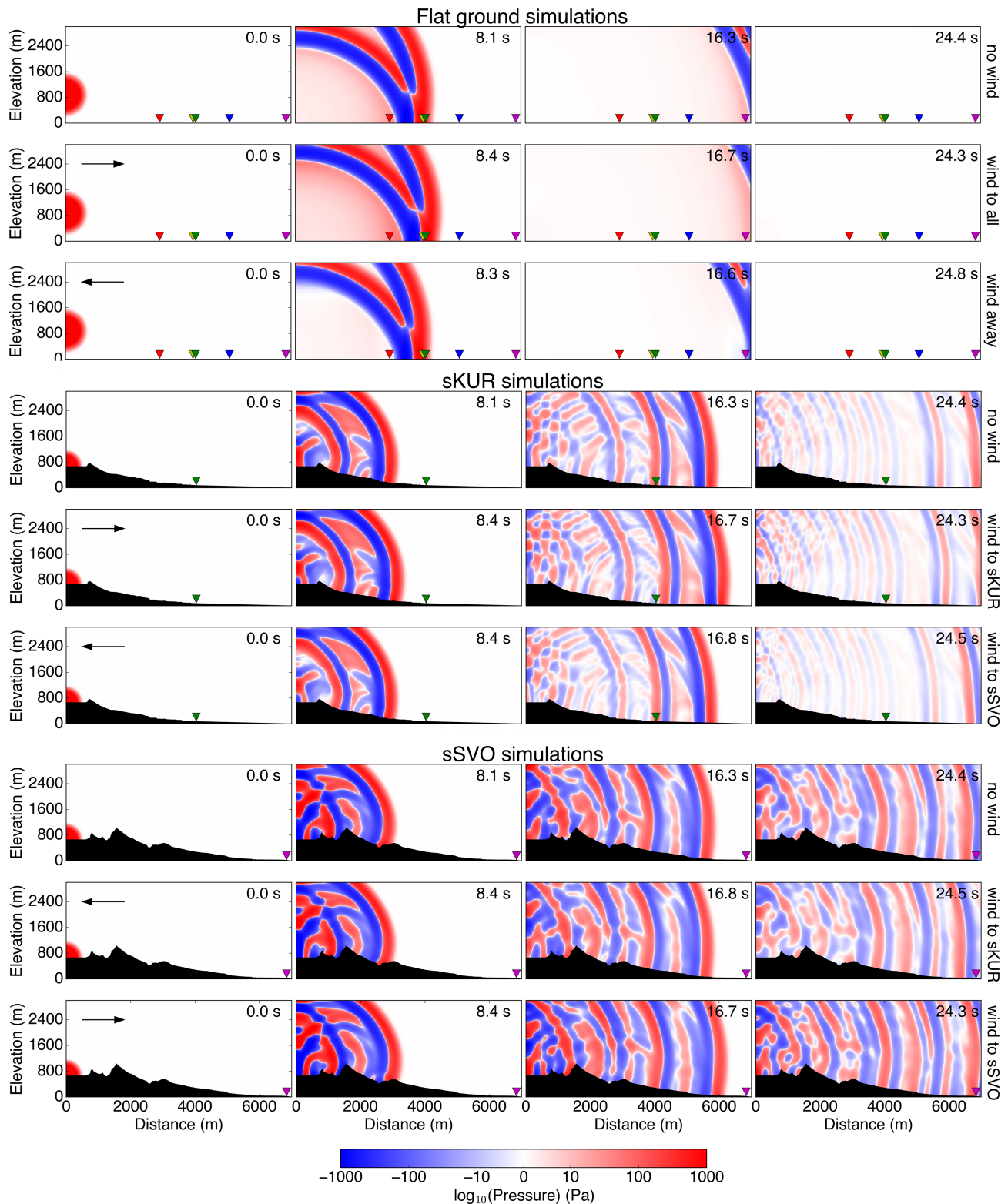


Figure 6. Wavefield snapshots for nonlinear acoustic propagation simulations over flat ground, Sakurajima station KUR topography, and station SVO topography using the method of de Groot-Hedlin (2017). Each row shows snapshots advancing in time from left to right for one lower boundary type and one wind condition. Triangles indicate synthetic receiver locations (“s” for synthetic). Text at right and arrows (where applicable) indicate the wind condition (see Figure 5 for wind profiles). The first three rows represent simulations over flat ground in Simulation Sets S1, S7, and S8 in Table 1. The middle three rows represent simulations over KUR topography in Sets S1, S5, and S6. The lower three rows represent simulations over SVO topography in Sets S1, S5, and S6.

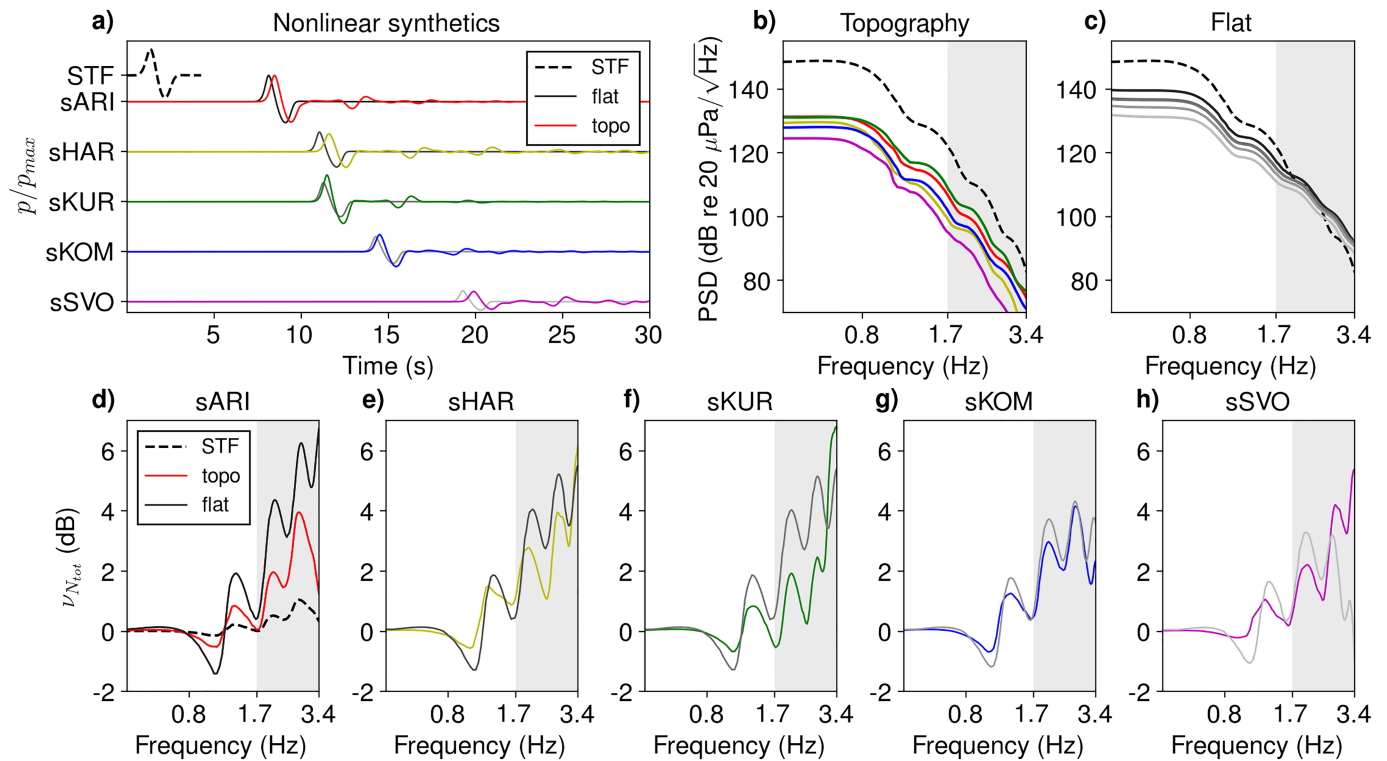


Figure 7. (a) Synthetic (“s”) waveforms from windless nonlinear FDTD Simulation Set S1 in Table 1. Colored waveforms correspond to simulations with Sakurajima topography and receivers at Sakurajima station distances. Solid grayscale waveforms correspond to simulations over flat ground with receivers at slant station distances. The dashed black line shows the approximate source time function normalized by the maximum amplitude as described in the caption for Figure 4a and text. The other waveforms are normalized by the peak pressure at sARI (p_{max}). (b) PSD estimates for the synthetic waveforms from Sakurajima topography simulations in Figure 7a. Tukey-tapered time windows of 31 s each are used, with 7 s before and 24 s after peak pressure. Colors correspond to stations as shown in Figure 7a while the dashed line corresponds to the STF. (c) PSD estimates for the synthetic waveforms from flat ground simulations in Figure 7a. Grayscale lines correspond to stations as shown in Figure 7a while the dashed line corresponds to the STF. (d–h) Cumulative v_N estimates ($v_{N_{tot}}$) for spectra from topography and flat ground simulations for each station (colored and grayscale, respectively). The gray shaded regions indicate frequency components above 1.7 Hz for which synthetic spectra may be inaccurate due to numerical dispersion.

propagation over flat ground results in generally greater-magnitude $v_{N_{tot}}$ spectra relative to windless or downwind propagation (Figures 8f–8j).

When topography is included, the $|v_{N_{tot}}|$ levels are reduced compared to flat ground results as discussed in section 4.1, and downwind propagation conditions (red lines in Figure 8) generally result in smaller-magnitude $v_{N_{tot}}$ levels than upwind conditions (blue lines in Figure 8). We tentatively interpret this result (section 5.2) as a consequence of enhanced multipathing in the downwind direction that results in multiple arrivals that obscure the nonlinearly generated phase coupling from wave steepening. However, each of these combinations of wind and topography yield a $v_{N_{tot}}$ spectrum with the reclined S shape in general agreement with previous studies (Miller & Gee, 2018) and theory (Reichman et al., 2016). These results show that neither topography nor wind is sufficient to explain the complexity of $v_{N_{tot}}$ for the observed Sakurajima signals as shown in Figures 4g–4k and discussed in section 4.4.

4.3. Influence of Source Amplitude on Modeled v_N Results

Since the strength of nonlinear wavefield changes (e.g., wave steepening and period lengthening) is thought to increase with amplitude, we hypothesize that the magnitude of v_N will increase with source pressure. We test this by running eight simulations with source pressures ranging from 1.5 to 95 kPa and receivers placed within 1 km from the edge of the source radius (section 3.2). The results clearly show that larger source pressures lead to greater waveform asymmetry with increasing distance (Figure 9a) and enhanced power spectral density at higher frequencies (Figures 9b–9f and 9l–9p). The magnitude of $v_{N_{tot}}$ generally increases with source pressure (Figures 9g–9k and 9q–9u); for example, the absolute values of $v_{N_{tot}}$ at 1.7 Hz as recorded at 313 m are 0.08, 0.12, 0.11, 0.07, 0.12, 0.16, and 0.34 dB for source pressures of 1.5, 2.7, 5.9, 11.9, 23.8, 35.6, 47.5, and 95.0 kPa, respectively. A degree of frequency-dependent variability and complexity is present in

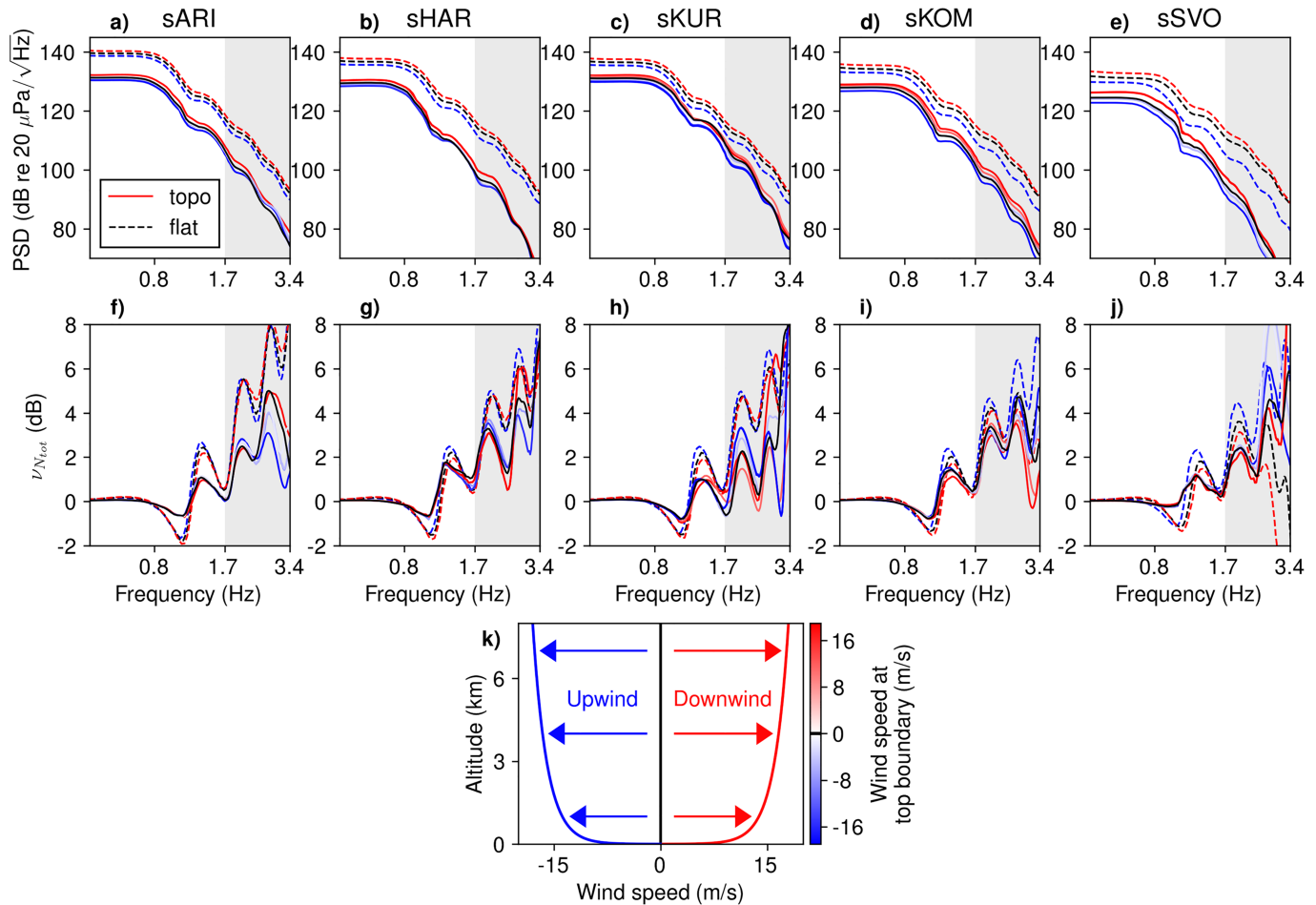


Figure 8. (a–e) Synthetic PSD results from simulations with different wind conditions (Simulation Sets S1–S8) plotted by synthetic receiver (“s” for synthetic). Each line represents the spectrum for a different wind condition as recorded at the receiver in the subplot title. Colors represent wind speed at the upper boundary for the simulation as illustrated in Figure 8k. Results from the windless simulations (Set S1) are shown in black for clarity. Solid lines show results from simulations with topography (Sets S1–S6) while dashed lines are from simulations with flat ground (S1, S7, and S8). The gray shaded region indicates frequency components above 1.7 Hz for which synthetic spectra may be inaccurate due to numerical dispersion. (f–j) Cumulative nonlinearity indicator results ($v_{N_{tot}}$) for the PSDs above. (k) Example wind speed profiles to illustrate the color implementation. Red colors indicate wind blowing toward a station (downwind propagation) and blue colors indicate wind blowing away (upwind propagation). Arrows indicate the corresponding wind direction in the source–receiver plane.

the relationships between $v_{N_{tot}}$ magnitude, source pressure, and distance, but the general trend shows that larger source pressures lead to greater nonlinear changes that can be detected with $v_{N_{tot}}$. Conversely, $v_{N_{tot}}$ tends towards zero for reduced source pressures that yield smaller nonlinear changes.

Inconsistencies in the relationships between source pressure, distance, $v_{N_{tot}}$ magnitudes, and the frequencies of $v_{N_{tot}}$ maxima and minima (Figures 9g–9k and 9q–9u) may reflect the highly nonlinear process by which spectral energy is transferred. For example, at 916 m the value of $v_{N_{tot}}$ is greater for a 47.5-kPa source than a 95.0-kPa source (0.64 and 0.37 dB), respectively. However, since spectral energy is transferred to progressively higher-frequency components with distance (e.g., Hamilton & Morfe, 2008), we speculate that the wave from a 95.0-kPa source may be primarily transferring more energy to a higher-frequency component at 916 m, while from a 47.5-kPa source may transfer more energy to 1.7 Hz. Since these simulations are only reliable at frequencies ≤ 1.7 Hz (section 3.2), we cannot confirm this with confidence. Further work outside the scope of this study could investigate the change in $v_{N_{tot}}$ with distance over a broader frequency range.

4.4. Observed $v_{N_{tot}}$ Results

Application of the $v_{N_{tot}}$ indicator to 30 eruptive events in the Sakurajima data set reveals cumulative distortions ranging from -10.4 to 10.1 dB in the 0.1- to 10-Hz frequency range (Figures 10a and 10c). However, most events feature cumulative $v_{N_{tot}}$ changes on the order of $\leq 10^{-1}$ dB, and the shapes of the observed indicator

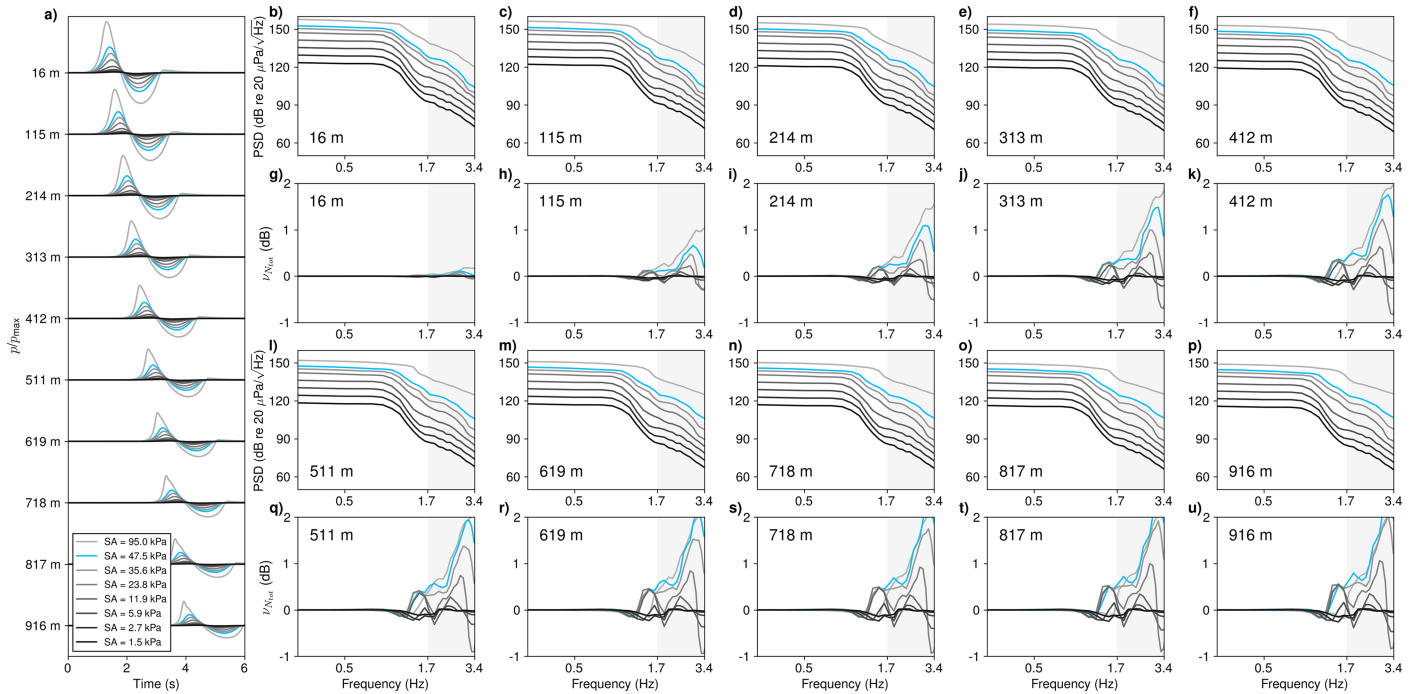


Figure 9. (a) Synthetic waveforms for Simulation Set S10 (Table 1) recorded at 10 receivers for eight different maximum source pressures. Blue lines show results for the source pressure used in Simulation Sets S1–S9. (b–f) Power spectral density for eight different source pressure conditions at five receivers with range of 16–412 m from the edge of the source radius. (g–k) Cumulative nonlinearity indicator ($v_{N_{tot}}$) curves for the spectra in Figures 9b–9f. (l–p) Power spectral density for eight different source pressure conditions at five receivers with range of 511–916 m from the edge of the source radius. (q–u) Cumulative nonlinearity indicator ($v_{N_{tot}}$) curves for the spectra in Figures 9l–9p. The gray shaded regions indicate frequency components above 1.7 Hz for which synthetic spectra may be inaccurate due to numerical dispersion.

spectra do not exhibit the reclined S shape observed in previous studies (Figure 1c; ; Miller & Gee, 2018) or our numerical modeling results (Figures 4g–4k). In many cases, observed $v_{N_{tot}}$ is generally positive above 1 Hz (e.g., Figures 3d and 3h) without proportional negative values at lower frequencies. We note here that a meaningful v_N spectrum need not sum to 0 due to the logarithmic scale of the indicator (e.g., Falco et al., 2006; Miller & Gee, 2018); however, the observed Sakurajima $v_{N_{tot}}$ results are clearly lacking in proportional losses at low frequencies seen in previous work (e.g., Figure 1c; ; Miller & Gee, 2018).

The lack of expected structure in the v_N spectra is reflected in the metrics (Figure 10). Peak signal pressure has a weak positive correlation with maximum $v_{N_{tot}}$ (Figure 10a) and weak negative correlation with minimum $v_{N_{tot}}$ (Figure 10c). We expect these correlations based on the theory that nonlinear effects become stronger with increasing signal pressure. However, there is no correlation between the frequencies of maximum and minimum $v_{N_{tot}}$ (Figure 10b), or between $v_{N_{tot}}$ and f_c (Figure 10d). The gray shading in Figure 10b indicates a region where metric values are not expected according to theory, since energy is expected to primarily transfer upward in the spectrum, yielding a greater frequency of maximum $v_{N_{tot}}$ than the frequency of minimum $v_{N_{tot}}$. The occurrence of results in this region indicates that the observed v_N behavior does not agree with expectations from theory and previous work (e.g., Miller & Gee, 2018). The general occurrence in Figure 10d of $v_{N_{tot}} > 0$ values at the centroid frequency may reflect period lengthening and/or shock coalescence below the peak source frequency of the source process; however, the scatter and low-magnitude values suggest that this feature is less significant than upward spectral energy transfer by wave steepening.

The general scatter and weak correlations in these metrics could indicate that acoustic propagation is linear, or that near-source nonlinearity is present but the associated spectral energy transfer is not accurately quantified by the v_N indicator. We suggest in the following section that v_N reveals potentially significant nonlinear spectral energy transfer but that the effects are poorly resolved in this data set due to complicating factors arising from source and propagation processes.

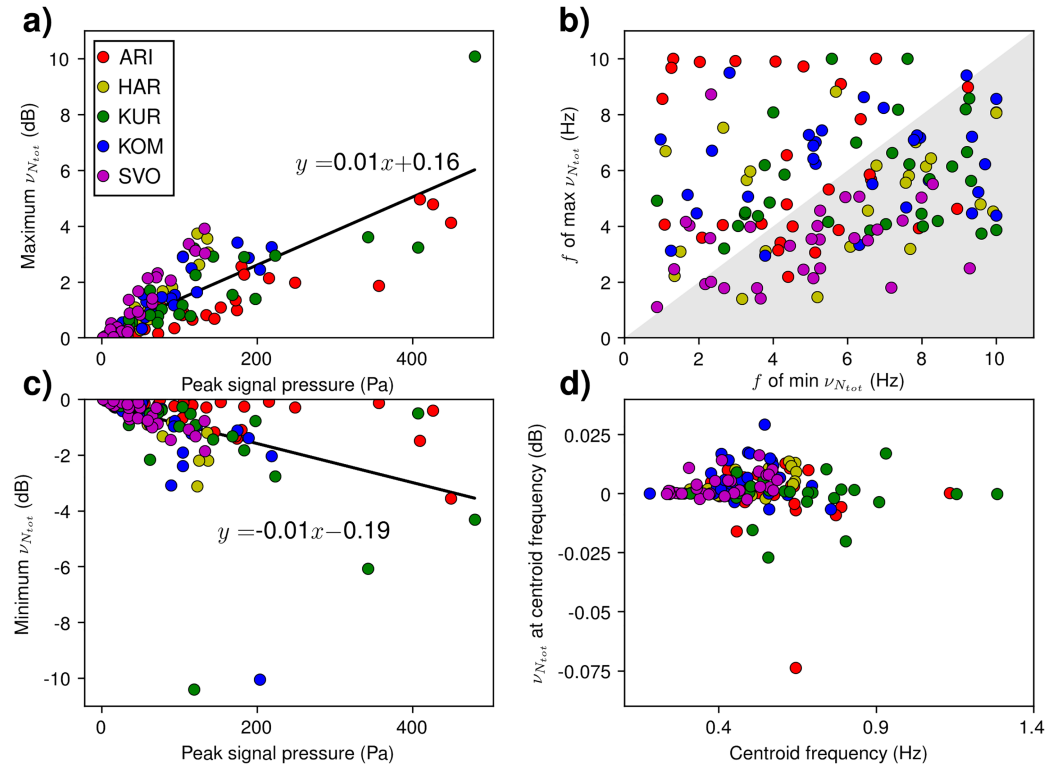


Figure 10. Nonlinearity indicator metrics for 30 high-SNR eruption events out of 74 in the Matoza et al. (2014) catalog. All $\nu_{N_{tot}}$ spectra are integrated with respect to station slant distance (rd). (a) Maximum cumulative $\nu_{N_{tot}}$ as a function of maximum signal pressure. Black line and equation represent a linear least squares fit. (b) Frequency of maximum $\nu_{N_{tot}}$ plotted against the frequency of the minimum $\nu_{N_{tot}}$. Gray shaded region represents area of parameter space where results are not expected based on theory (see text and Figure 1c). (c) Minimum cumulative ν_N as a function of maximum signal pressure. (d) $\nu_{N_{tot}}$ at the centroid frequency versus the value of the centroid frequency. Not shown is an outlier of $\nu_{N_{tot}} = 0.23$ dB at $f_c = 0.99$ Hz. All colors correspond to stations as per legend in Figure 10a.

5. Discussion

Application of a quadspectral density nonlinearity indicator to 30 Sakurajima acoustic eruption signals yields results suggestive of spectral energy transfer due to nonlinear wave steepening, while finite-difference propagation modeling unambiguously produces up to 2 dB of spectral energy transfer in the cases considered. Wavefield interactions with wind and topography modify the synthetic ν_N levels; however, neither wind nor topography are sufficient to explain the differences between observed Sakurajima ν_N spectra and expectations based on theory and previous studies. These results could indicate that acoustic propagation from Sakurajima volcano is linear at the distances considered; however, evidence from previous studies (Ishihara, 1985; Yokoo & Ishihara, 2007) and our nonlinear propagation modeling (section 4.1) suggests that nonlinear changes to the wavefield may occur near the source. We suggest that nonlinear acoustic propagation effects may be significant at Sakurajima, but the ν_N indicator does not accurately quantify the spectral energy transfer in the observed signals because of complications from complex source dynamics and outdoor propagation effects.

5.1. Quantifying Spectral Energy Transfer in Sakurajima Acoustic Eruption Signals

Comparison of the cumulative effects of nonlinear propagation ($\nu_{N_{tot}}$) on synthetic Sakurajima signals to other distorting processes (Figure 11) shows that spectral energy transfer is less significant than the effects of geometrical spreading ($\nu_{S_{tot}}$) but more significant than atmospheric absorption ($\nu_{\alpha_{tot}}$). The frequency-dependent absorption losses are calculated using the approaches of Bass et al. (1984) and Sutherland and Bass (2004) as described in Appendix 2. This indicates that corrections for nonlinear spectral energy transfer may provide a significant second-order improvement in accuracy for acoustically based source parameter estimates. However, the disagreement between observed Sakurajima $\nu_{N_{tot}}$ and the ν_N behavior seen in previous studies (Reichman et al., 2016; Miller & Gee, 2018) and our numerical modeling (section

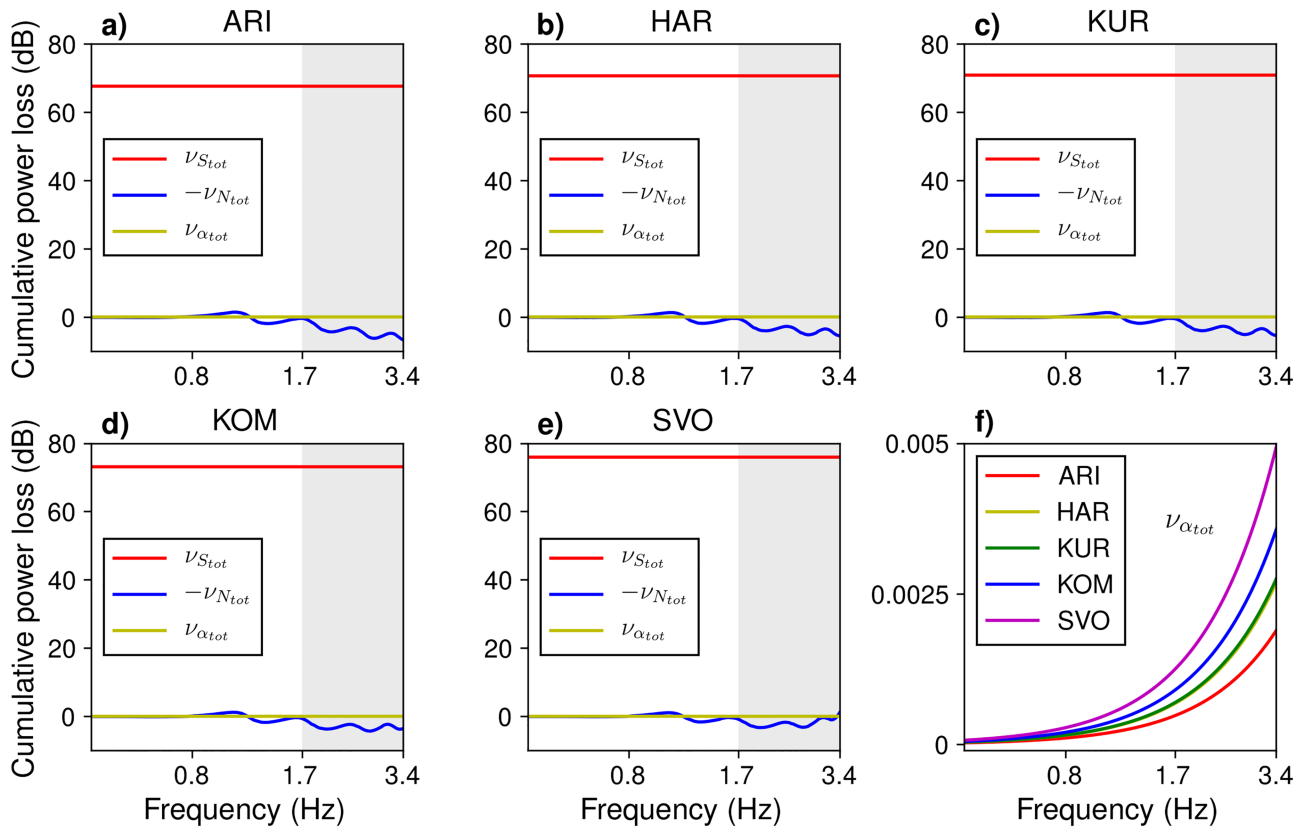


Figure 11. (a–e) Comparisons of cumulative spectral power losses due to geometrical spreading ($v_{S_{tot}}$), absorption ($v_{\alpha_{tot}}$), and nonlinear effects ($v_{N_{tot}}$). The $v_{N_{tot}}$ results shown are from nonlinear, windless flat ground simulations (S1 in Table 1), and the sign of $v_{N_{tot}}$ is flipped ($-v_{N_{tot}}$) to be consistent with the other spectra (i.e., positive values indicate power loss). Note that losses to spherical spreading ($v_{S_{tot}}$) are frequency-independent, while losses to absorption depend on frequency, but are too small to see at the scale of plots Figures 11a–11e. The gray shaded region indicates frequency components above 1.7 Hz for which synthetic spectra may be inaccurate due to numerical dispersion. (f) Frequency dependence of $v_{\alpha_{tot}}$ at each station. Calculation of $v_{\alpha_{tot}}$ and $v_{S_{tot}}$ are described in Appendix A.

4.1 and 4.2) suggest that the nonlinearity indicator does not accurately quantify spectral energy transfer in this data set.

The large magnitudes of observed $v_{N_{tot}}$ results (up to ~ 10 dB) suggest that nonlinear propagation effects may be significant, but the inconsistencies in the shapes of the observed $v_{N_{tot}}$ spectra (Figures 3d and 3h) and poorly correlated $v_{N_{tot}}$ metrics (Figure 10), indicate that v_N does not accurately resolve nonlinear effects in the Sakurajima data set. We suggest that v_N does not accurately quantify these effects because of complications from source and propagation dynamics. While the assumptions underlying the v_N equation (see sections 1.1 and Appendix ?) can be reasonably met for computational propagation of the Burgers equation in the free field (Reichman et al., 2016), and for model-scale jet noise propagation in an anechoic chamber (Miller & Gee, 2018), they are violated in the context of complex source processes and outdoor propagation effects. Volcano-acoustic spectra are affected by contributions from wavefield interactions with topography (reflections, diffraction, and scattering), refraction in local wind and temperature gradients, and nonlinear source dynamics with multiphase fluid flow, turbulent jetting, and impulsive explosions (e.g., Matoza et al., 2019). For example, it is possible that combinations of broadband power from explosions with lower-frequency jet noise may be treated by v_N as spectral gains at high frequencies without corresponding losses at lower frequencies (e.g., Figure 3h).

5.2. Influence of Topography and Wind on v_N

To investigate the effects of outdoor acoustic propagation on v_N , we isolate the effects of topography by comparing synthetic results between numerical simulations with topography and with flat ground, and we isolate the effect of wind by comparing results between windless simulations and those with a variety of

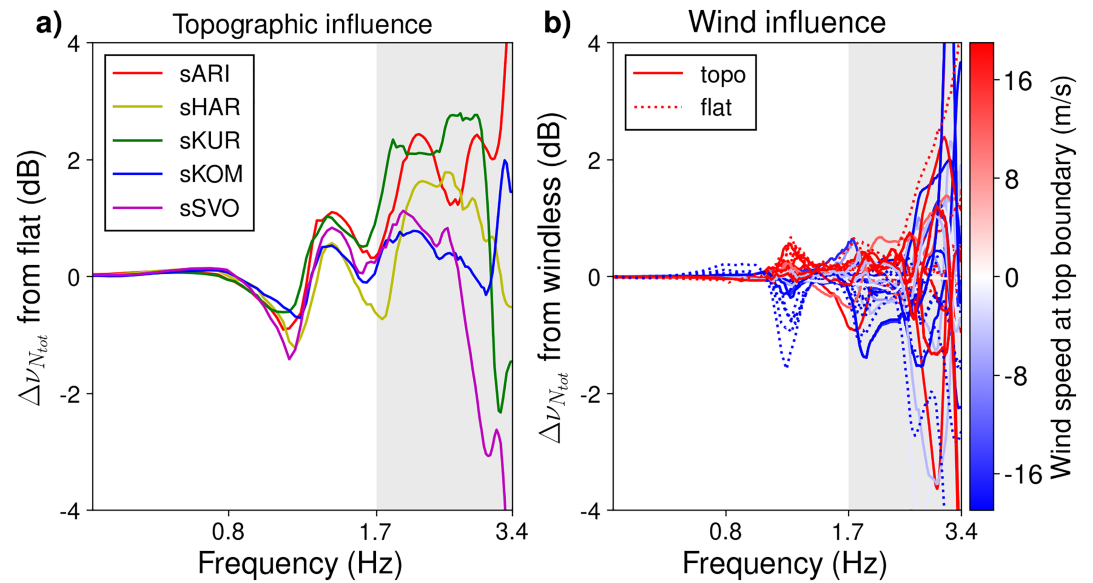


Figure 12. (a) Topographic influence on $v_{N_{tot}}$ as expressed by the difference in $v_{N_{tot}}$ from FDTD simulation results with flat ground and with topography (i.e., $\Delta v_{N_{tot}} = \text{flat result} - \text{topography result}$). The gray shaded region indicates frequency components above 1.7 Hz for which synthetic spectra may be inaccurate due to numerical dispersion. (b) Influence of wind on $v_{N_{tot}}$ as expressed by the difference in $v_{N_{tot}}$ from FDTD simulation results with and without wind (i.e., $\Delta v_{N_{tot}} = \text{windless result} - \text{windy result}$). Solid lines indicate results from simulations with topography, while dashed lines indicate results from simulations with flat ground. Colors correspond to the wind speed at the top boundary of the model space as shown in Figure 8k.

wind conditions (Table 1). We find that these effects create v_N variations that modify the nonlinear signature, but neither process is sufficient to explain the departure of observed v_N from modeling results.

Inclusion of topography in nonlinear simulations reduces $|v_N|$ levels compared to propagation over flat ground (Figures 7d–7h). One potential explanation for this is preferential attenuation of high-frequency components due to acoustic scattering and reflection from topography. These losses counteract gains at high frequencies due to nonlinear wave steepening and lead to underestimation of spectral energy transfer by v_N . Additionally, the nonlinearly generated phase coupling quantified by Q_{pp^2} is obscured by offsets in phase between multipathed arrivals from various raypaths reflected from topography.

In contrast, wind differentially affects PSD and v_N . Figure 8 shows that PSD is greater, while $v_{N_{tot}}$ levels are lower at downwind stations compared to upwind. We interpret this behavior as a result of downwind-waveguiding that causes acoustic waves to multiply reflect from the ground and the inverted sound speed gradient (Bies et al., 2017; Pierce, 1981). This process may cause offsets in arrival times of the reflected waves that cause phase shifts that artificially obscure the phase coupling induced by nonlinear propagation. Thus, downwind spectra may have relatively low-magnitude v_N levels because the quad spectrum (Q_{pp^2}) cannot recover the coupled harmonics that are offset in arrival time.

In the true outdoor case, reflection from ground with finite-impedance or with near-surface air turbulence excited by solar heating can produce additional frequency-dependent phase shifts (Bies et al., 2017; Pierce, 1981) that may further obscure the phase coupling. The effects of impedance on low-frequency sound waves are small (Embleton et al., 1976; Piercy et al., 1977) and thus typically neglected in infrasound research (e.g., Bass, 1991; Sutherland & Bass, 2004; Whitaker & Norris, 2008). Rigid lower boundary conditions have been previously used to achieve strong agreement between observed and synthetic waveforms (e.g., Fee et al., 2017; Kim & Lees, 2011; Kim et al., 2015; Lacanna & Ripepe, 2013), suggesting that the effects of finite impedance are negligible. However, low ground impedance due to loose tephra layers or shallow hydrother-

mal alteration (e.g., Matoza et al., 2009) may be significant in the context of phase shifts upon reflection. This process is not accounted for in our FDTD simulations because the lower boundary is rigid such that phase is preserved on reflection. The effects of phase shifting on reflection of infrasound from finite-impedance ground could be a direction for future research outside the scope of this study.

To compare the relative magnitudes of topographic and wind effects on v_N , we calculate differences in v_N spectra between results from topography simulations and results from flat ground simulations (S1), and between windy simulations and windless simulations (S1–S8). Figure 12 shows the results of these analyses, where the dependent variables are $\Delta v_{N_{tot}}$ from flat (Figure 12a) and $\Delta v_{N_{tot}}$ from windless (Figure 12b). Larger amplitudes for $\Delta v_{N_{tot}}$ from flat indicate that the effect of topography is more significant than that of wind, and that effect is to reduce $|v_N|$. The smaller effect of wind depends on wind direction as discussed above.

We conclude that frequency-dependent distortions from wavefield interactions with topography and wind may inhibit the effectiveness of the v_N indicator by modifying the signature of spectral energy transfer due to wave steepening. Differences between observed Sakurajima v_N and modeling results may be due to additional complications from finer-scale meteorological structures (e.g., convective winds in canyons) and/or spectral contributions from complex source dynamics. Our modeling work has been limited to a simplistic Gaussian acoustic source function yielding nearly symmetrical waveforms that poorly match observations (Figure 4), but recent work with fluid-dynamical sources have modeled asymmetrical waveforms even with linear acoustic propagation (Brogi et al., 2018; Cerminara et al., 2016). Three-dimensional wavefield effects are also likely significant, as our approach is limited to a 2-D axisymmetric cylindrical geometry. For example, Kim et al. (2015) used linear 3-D FDTD modeling to produce synthetic pressure waveforms in strong agreement with observed Sakurajima infrasound; however, their model did not test the effects of nonlinear wave steepening. We suggest that future v_N applications may therefore be more successful in the presence of simpler topography for which 3-D effects are less significant, and with more realistic source-time functions for numerical modeling. Despite these limitations, our approach is sufficient to show that wavefield interaction with topography reduces the amplitude of the v_N indicator. The true reduction in the presence of 3-D topography may be greater.

We note here that these results may also be interpreted as an indication that nonlinear effects are insignificant for Sakurajima acoustic signals and that consequently the linear propagation assumption is reasonable for estimating source parameters such as volume and mass flux (e.g., Fee et al., 2017; Johnson & Miller, 2014; Kim et al., 2015) or gas exit velocity (e.g., Matoza et al., 2013; McKee et al., 2016; Woulff & McGetchin, 1976). However, the potential significance of nonlinear effects at Sakurajima is evidenced by observations of supersonic wave propagation (Ishihara, 1985; Yokoo & Ishihara, 2007) asymmetric pressure waveforms (e.g., Matoza et al., 2014), and acoustically based source parameters that underestimate (Johnson & Miller, 2014) or overestimate (Fee et al., 2017) values obtained by other methods. We tentatively conclude that the indicator is strongly influenced by additional outdoor propagation effects such as phase shifts on reflection from finite-impedance ground, and complex source dynamics including turbulent jet noise and fluid flow following an initial explosion. These source and propagation effects are not accounted for in the nonlinearity indicator analysis or in our numerical modeling approach, and they therefore complicate the ability to resolve nonlinear spectral energy transfer. Future investigations of nonlinear propagation effects may therefore be more conclusive in applications to data collected at close range to the vent (e.g., <2 km) on volcanoes with low-relief topography, large source amplitudes, and simple source-time functions (e.g., gas-rich strombolian explosions).

6. Conclusion

We investigated the suitability of a quadspectral density-based nonlinearity indicator (v_N) developed by Reichman et al. (2016) for quantifying distortions to local volcano infrasound by spectral energy transfer during nonlinear acoustic propagation. We hypothesized that wave steepening during near-source nonlinear acoustic propagation causes significant energy transfer from the spectral peak of the source process to higher frequencies, and that wavefield interactions with topography and wind complicate the quantifiable signature of this process. Application of v_N to 30 acoustic eruption signals in an 8-day data set at Sakurajima Volcano, Japan, suggests cumulative nonlinear spectral distortions on the order of $< 10^1$ dB re 20 μ Pa, but the nonlinear signature, if present, is modified by complications from source processes and outdoor prop-

agation dynamics. To investigate the effects of topography and wind on v_N , we model nonlinear acoustic propagation over Sakurajima topography using a FDTD method (de Groot-Hedlin, 2017).

The results of acoustic propagation simulations indicate that v_N is indeed capable of detecting cumulative nonlinear spectral energy transfer on the order of 2 dB below 1.7 Hz at Sakurajima station distances and that wind and topography influence the indicators behavior. However, neither wind nor topography is sufficient to explain the observed complexity in v_N behavior for the Sakurajima signals; we suggest that fine-scale propagation effects (e.g., wave interaction with local winds and temperature gradients) and/or source dynamics (e.g., fluid flow and gas-particle interactions) distort the nonlinear signature. This approach to quantifying nonlinear spectral energy transfer may therefore be more conclusive for data sets collected with simpler volcano-acoustic source-receiver geometries. Accounting for the effect of spectral energy transfer may provide a second-order improvement in accuracy of source spectral estimates compared to the commonly used geometrical spreading correction.

Appendix A: Derivation and Integration of Nonlinear Propagation Equation

The following discussion summarizes derivations by Morfey and Howell (1981) and Reichman et al. (2016) of a quadspectral density-based nonlinearity indicator. Derivation of the Generalized Burgers Equation from the 1-D plane wave equation is primarily summarized from Hamilton and Morfey (2008).

Acoustic waves are pressure disturbances to the ambient state of a material with properties governed by the fundamental conservations of mass, momentum, entropy, and thermodynamic state. The propagation of a pressure disturbance p in one dimension can be written as follows:

$$\frac{\partial^2 p}{\partial x^2} - \frac{1}{c^2} \frac{\partial^2 p}{\partial t^2} = 0 \quad (\text{A1})$$

where p is traveling in the x direction with sound speed c over time t (Pierce, 1981). This second-order partial differential equation describes linear plane wave propagation in the absence of dispersion and losses to the medium. To account for the effects of nonlinear propagation (dispersion) and losses to the medium (dissipation), an approximation to equation (A1) must be made.

A second-order approximation can be made by substituting the first two terms of the Taylor series expansion of the pressure-density relationship $\left(\frac{p}{\rho_0} = \left(\frac{p}{\rho_0}\right)^\gamma\right)$, where γ is the ratio of specific heats) into the equations of continuity, momentum, and state, and by neglecting Lagrangian density ($\mathcal{L} = \frac{1}{2}\rho_0 u^2 - \frac{p^2}{2\rho_0 c_0^2}$), which is equal to 0 for plane progressive waves (Hamilton & Morfey, 2008). This gives the Westervelt equation:

$$\frac{\partial^2 p}{\partial x^2} - \frac{1}{c_0^2} \frac{\partial^2 p}{\partial t^2} + \frac{\delta}{c_0^4} \frac{\partial^3 p}{\partial t^3} = -\frac{\beta}{\rho_0 c_0^4} \frac{\partial^2 p^2}{\partial t^2}, \quad (\text{A2})$$

where δ is a thermoviscous coefficient describing sound diffusion in air, $\delta = \frac{1}{\rho_0} \left(\frac{4}{3}\mu + \mu_B\right) + \frac{\kappa}{\rho_0} \left(c_v^{-1} - c_p^{-1}\right)$, where ρ_0 is ambient density, μ is shear viscosity, μ_B is bulk viscosity, κ is thermal conductivity, c_v is isochoric specific heat and c_p is isobaric specific heat, and β is a nondimensional dispersion (nonlinearity) coefficient in air (Hamilton & Morfey, 2008). The nonlinearity coefficient β is an intrinsic quantity to the medium that characterizes the effect of finite-amplitude wave propagation on sound speed (Hamilton & Blackstock, 2008). The relationship to sound speed can be written as $c = c_0 \left(1 + \frac{\beta p}{\rho_0 c_0^2}\right)$, such that larger values of β and p result in larger increases in speed (Hamilton & Blackstock, 2008). In air, $\beta \approx 1.2$ and can be written as a function of the ratio of specific heats, $\beta = \frac{1}{2}(\gamma + 1)$, where $\gamma = c_p/c_v$ (Hamilton & Blackstock, 2008).

Simplification of the Westervelt equation into one dimension (a forward-propagating plane wave) and a retarded time scale ($\tau = t - x/c_0$) yields the Burgers equation:

$$\frac{\partial p}{\partial x} - \frac{\delta}{2c_0^3} \frac{\partial^2 p}{\partial \tau^2} = \frac{\beta p}{\rho_0 c_0^3} \frac{\partial p}{\partial \tau}, \quad (\text{A3})$$

which predicts waveforms as a function of distance and time for plane wave propagation with nonlinear effects and diffusion in a thermoviscous medium. Generalization of the Burgers equation to spherical and cylindrical waves is achieved by addition of a geometrical spreading term:

$$\frac{\partial p}{\partial r} + \frac{m}{r}p - \frac{\delta}{2c_0^3} \frac{\partial^2 p}{\partial \tau^2} = \frac{\beta p}{\rho_0 c_0^3} \frac{\partial p}{\partial \tau}, \quad (\text{A4})$$

where r is now source-receiver distance and $m = 0, 0.5,$ or 1 for planar, cylindrical, or spherical waves, respectively. Equation (A4) is the Generalized Burgers Equation. Transformation of the Generalized Burgers Equation into the frequency domain gives

$$\frac{\partial \tilde{p}}{\partial r} + \frac{m}{r}\tilde{p} - \frac{\omega\delta}{2c_0^3}\tilde{p} = \frac{i}{2} \frac{\beta}{\rho_0 c_0^3} \omega \tilde{q}, \quad (\text{A5})$$

where \tilde{p} and \tilde{q} are the complex Fourier transforms of $p(\tau)$ and $p^2(\tau)$, respectively (Morfey & Howell, 1981). Multiplication of equation (A5) by r^m , simplification, and substitution of $\omega^2\delta/2c_0^3$ for α' (a combination of dispersion and linear attenuation coefficients, where the linear absorption coefficient of sound is $\alpha = \text{Re}\{\alpha'\}$) yields:

$$\left(\frac{\partial}{\partial r} + \alpha'\right)r^m\tilde{p} = \frac{i}{2} \frac{\beta\omega}{\rho_0 c_0^3} r^m\tilde{q}, \quad (\text{A6})$$

which is equivalent to equation 3 of Morfey and Howell (1981) and equation 5 of Reichman et al. (2016). Equation (A6) is valid for sound of moderate intensity (≤ 165 dB = 3,557 Pa) recorded in the far field ($r > \lambda$) with weak attenuation and dispersion ($|\alpha'| \ll \omega/c$) and weak nonlinearity (Morfey & Howell, 1981). Furthermore, equation (A6) is deterministic in that it can ostensibly be used to predict spectra rather than to statistically describe spectral changes from a single measurement. The statistical form is derived by multiplying equation (A6) through by r and by the complex conjugate of \tilde{p} , then ensemble averaging the real part to give

$$\frac{\partial}{\partial r} (r^{2m} e^{2\alpha r} S_{pp}) = -\frac{\beta\omega}{\rho_0 c_0^3} r^{2m} e^{2\alpha r} Q_{pp^2}, \quad (\text{A7})$$

where S_{pp} is the autospectral density of p and Q_{pp^2} is the quadspectrum of p and p^2 , which is the imaginary part of the cross-spectral density between p and p^2 . The term on the left-hand side represents the spatial rate of change in the power spectral density of a spreading wave and should be equal to 0 if the propagation is linear because the spectrum is corrected for geometrical spreading and absorption. Nonlinear propagation effects are represented by nonzero values of the right-hand side of this equation. The nonlinearity coefficient β describes the intrinsic nonlinear property of the medium (change in sound speed due to finite-amplitude effects). Q_{pp^2} describes phase coupling between p and p^2 during spectral energy transfer to higher harmonics. Phase coupling arises from the summing and differencing of frequency components as a wave steepens and spectral energy is transferred between frequencies (Kim & Powers, 1979). The quadspectrum highlights phase-coupled frequencies because individual harmonic components of p^2 can be mathematically represented as a sum of the products between all individual pairwise harmonics of p ; the phase information of the Fourier-transformed cross-covariance function of p and p^2 consequently peaks in absolute value when harmonics are phase-coupled (Gagnon, 2011).

Equation (A7) gives a qualitative indication of which frequencies gain and lose energy during nonlinear propagation, but it does not give quantitative estimates of the amount of power transfer. To make the Morfey and Howell (1981) formulation more quantitative, Reichman et al. (2016) manipulate equation (A7) to give the spatial rate of change in spectral level, $\frac{\partial L_p}{\partial r}$, where L_p is the spectral level in an arbitrary frequency band ($L_p = 10 \log_{10}(p_i^2/p_{ref}^2)$), where p_i is pressure in an arbitrary frequency band and p_{ref} is a reference pressure, typically 20 μ Pa). They start by expanding the derivative on the left-hand side of equation (A7) using the product rule, dividing by $r^{2m} e^{2\alpha r} S_{pp}$, and moving terms to give

$$\frac{1}{S_{pp}} \frac{\partial S_{pp}}{\partial r} = -\frac{2m}{r} - 2\alpha - \frac{\omega\beta p_{rms}}{\rho_0 c_0^3} \frac{Q}{S}, \quad (\text{A8})$$

where p_{rms} is root-mean-square pressure and Q/S is the normalized quadspectrum ($Q/S = Q_{pp^2}/S_{pp}p_{rms}$). A property of logarithms is then employed to consolidate the S_{pp} terms into the spatial derivative:

$$\frac{1}{S_{pp}} \frac{\partial S_{pp}}{\partial r} = \frac{\partial}{\partial r} \{ \ln(S_{pp}) \} = \frac{\partial}{\partial r} \left\{ \frac{\log_{10}(S_{pp})}{\log_{10}(e)} \right\}, \quad (\text{A9})$$

where e is Euler's number ($e \approx 2.71828$). The autospectral density of p is replaced using the identity $L_p = 10 \log_{10}(p^2/p_{ref}^2) = 10 \log_{10}(S_{pp}/P_{ref}^2)$:

$$\frac{\partial}{\partial r} \left\{ \frac{\log_{10}(S_{pp})}{\log_{10}(e)} \right\} = \frac{\partial}{\partial r} \left\{ \frac{1}{\log_{10}(e)} \left(\frac{L_p}{10} + 2 \log_{10}(P_{ref}) \right) \right\}, \quad (\text{A10})$$

Substituting equation (A10) into equation (A8), neglecting the p_{ref} term since it cancels upon differentiation, moving the e term, and cancelling the p_{rms} terms gives the desired result:

$$\frac{\partial L_p}{\partial r} = -10 \log_{10}(e) \left(\frac{2m}{r} + 2\alpha + \frac{\omega\beta}{\rho_0 c_0^3} \frac{Q_{pp^2}}{S_{pp}} \right), \quad (\text{A11})$$

which is the equation used in this study. This equations assumes that linear spectral changes can be fully described by v_s and v_a , neglecting potentially significant effects such as reflections from topography and refraction in temperature gradients. Spectral contributions from these processes are inaccurately treated by v_N as a consequence of nonlinear acoustic propagation. The ability of v_N to accurately describe nonlinear effects consequently depends on the complexity of the signal. Furthermore, while the equation was developed for analysis of acoustic signals of audible frequency (20-20,000 Hz), its basis in the Burgers equation dictates that it should be valid for any wave that steepens during propagation due to finite-amplitude effects. Nonlinear steepening of infrasonic waves is a well-established phenomenon at volcanoes (Lonzaga et al., 2015; Matoza et al., 2019), so we consider the application of equation (1) to Sakurajima data appropriate.

In this study we integrate equation (A11) with respect to distance to estimate the cumulative distortion effects over the source-receiver paths. This integration is performed as follows:

$$\begin{aligned} L_p &= -10 \log_{10}(e) \int_0^r \left(\frac{2m}{r} + 2\alpha + \frac{\omega\beta}{\rho_0 c_0^3} \frac{Q_{pp^2}}{S_{pp}} \right) dr \\ &= -10 \log_{10}(e) \left(2m \ln(r) + 2\alpha r + r \frac{\omega\beta}{\rho_0 c_0^3} \frac{Q_{pp^2}}{S_{pp}} \right) + C \\ &= -10 \log_{10}(e) \left(2m \ln(r) + 2\alpha r + r \frac{\omega\beta}{\rho_0 c_0^3} \frac{Q_{pp^2}}{S_{pp}} \right) + L_{p_0} \\ &\equiv v_{S_{tot}} + v_{\alpha_{tot}} + v_{N_{tot}} + L_{p_0}, \\ &\equiv v_{tot}, \end{aligned} \quad (\text{A12})$$

where the constant of integration C is equal to the level at the source (L_{p_0}) since no propagation changes occur at the source where $r = 0$, and the subscript *tot* indicates cumulative effects. The individual components of v_{tot} correspond to the elements of the equation as per equation (1). Integration assumes a constant rate of spectral change, when in fact the rate of change varies within the nonlinear propagation regime (Miller & Gee, 2018). Since Sakurajima stations are several kilometers from the source, observed $v_{N_{tot}}$ likely underestimates the total spectral changes.

In this study, $v_{N_{tot}}$ is estimated assuming an ambient sound speed of 349 m/s, ambient density of 1.225 kg/m³, and a nonlinearity coefficient of 1.201. v_s is estimated assuming spherical spreading since the wavelength of the dominant frequency (~ 873 m for 0.4 Hz) is significant relative to the receiver distances ($\sim 37\%$ of the closest receiver distance). v_a is estimated using the equations of Sutherland and Bass (2004) assuming average relative humidity (80%) and average temperature (28.5 °C) for Kagoshima City in July. This approach accounts for absorption due to molecular translation, rotation, vibrational relaxation of O₂ and N₂, and diffusion. We calculate the vibrational component using the equations of Bass et al. (1984), which is justified under the assumption that normalized relaxing specific heat $\ll 1$ for temperatures near sea level (Sutherland & Bass, 2004).

Acknowledgments

We thank Editor Martha Savage, an anonymous Associate Editor, and two anonymous reviewers whose comments led to improvements in the manuscript. We thank Tracianna Neilsen for helpful discussions about this project. The infrasound data from the 2013 Sakurajima deployment is publicly available through the IRIS DMC as described by Fee et al. (2014). The DEMs used in this study were provided by the Japanese Ministry of Land, Infrastructure, Transport and Tourism. This project was supported by NSF grants EAR-1620576 and EAR-1847736.

References

Anderson, J. F., Johnson, J. B., Steele, A. L., Ruiz, M. C., & Brand, B. D. (2018). Diverse eruptive activity revealed by acoustic and electromagnetic observations of the 14 July 2013 intense vulcanian eruption of Tungurahua Volcano, Ecuador. *Geophysical Research Letters*, *45*, 2976–2985. <https://doi.org/10.1002/2017GL076419>

Assink, J. D., Waxler, R., & Drob, D. (2012). On the sensitivity of infrasonic traveltimes in the equatorial region to the atmospheric tides. *Journal of Geophysical Research*, *117*, 1–14. <https://doi.org/10.1029/2011JD016107>

Atchley, A. A. (2005). Not your ordinary sound experience: A nonlinear-acoustics primer. *Acoustics Today*, *1*(1), 19–24. <https://doi.org/10.1121/1.2961122>

Bass, H. E. (1991). Atmospheric acoustics, *Encyclopedia of applied physics* (pp. 145–179). New York: VCH.

Bass, H. E., Sutherland, L. C., Piercy, J., & Evans, L. (1984). Absorption of sound by the atmosphere, *Physical acoustics volume xvii* (pp. 145–232). Orlando, Florida: Academic Press.

Berenger, J.-P. (1994). A perfectly matched layer for the absorption of electromagnetic waves. *Journal of Computational Physics*, *200*, 185–200. <https://doi.org/10.1006/jcph.1994.1159>

Bies, D. A., Hansen, C., & Howard, C. (2017). Sound propagation (5th ed.), *Engineering noise control* (pp. 59–86). Boca Raton: CRC Press, Taylor & Francis Group. <https://doi.org/https://doi.org/10.1201/9781351228152>

Bowman, J. R., Baker, G. E., & Bahavar, M. (2005). Ambient infrasound noise. *Geophysical Research Letters*, *32*, 1–5. <https://doi.org/10.1029/2005GL022486>

Brogi, F., Ripepe, M., & Bonadonna, C. (2018). Lattice Boltzmann modeling to explain volcano acoustic source. *Scientific Reports*, *8*(1), 9537. <https://doi.org/10.1038/s41598-018-27387-0>

Brown, D., Ceranna, L., Prior, M., Mialle, P., & Le Bras, R. J. (2014). The IDC seismic, hydroacoustic and infrasound global low and high noise models. *Pure and Applied Geophysics*, *171*(3–5), 361–375. <https://doi.org/10.1007/s00024-012-0573-6>

Buckingham, M., & Garcés, M. A. (1996). Canonical model of volcano acoustics. *Journal of Geophysical Research*, *101*(B4), 8129–8151. <https://doi.org/10.1029/95JB01680>

Caplan-Auerbach, J., Bellesiles, A., & Fernandes, J. K. (2010). Estimates of eruption velocity and plume height from infrasonic recordings of the 2006 eruption of Augustine Volcano, Alaska. *Journal of Volcanology and Geothermal Research*, *189*(1–2), 12–18. <https://doi.org/10.1016/j.jvolgeores.2009.10.002>

Cerminara, M., Esposti Ongaro, T., & Neri, A. (2016). Large eddy simulation of gas particle kinematic decoupling and turbulent entrainment in volcanic plumes. *Journal of Volcanology and Geothermal Research*, *326*, 143–171. <https://doi.org/10.1016/j.jvolgeores.2016.06.018>

Clarke, A. B., Esposti Ongaro, T., & Belousov, A. (2015). *Vulcanian eruptions* (Second). Elsevier Inc. <https://doi.org/10.1016/B978-0-12-385938-9.00028-6>

Dabrowa, A. L., Green, D. N., Rust, A. C., & Phillips, J. C. (2011). A global study of volcanic infrasound characteristics and the potential for long-range monitoring. *Earth and Planetary Science Letters*, *310*(3–4), 369–379. <https://doi.org/10.1016/j.epsl.2011.08.027>

Dalton, M. P., Waite, G. P., Watson, I. M., & Nadeau, P. A. (2010). Multiparameter quantification of gas release during weak Strombolian eruptions at Pacaya Volcano, Guatemala. *Geophysical Research Letters*, *37*, L09303. <https://doi.org/10.1029/2010GL042617>

de Groot-Hedlin, C. (2004). Criteria for discretization of seafloor bathymetry when using a staircase approximation: Application to computation of T-phase seismograms. *The Journal of the Acoustical Society of America*, *115*(3), 1103–1113. <https://doi.org/10.1121/1.1643361>

de Groot-Hedlin, C. D. (2016). Long-range propagation of nonlinear infrasound waves through an absorbing atmosphere. *The Journal of the Acoustical Society of America*, *139*(4), 1565–1577. <https://doi.org/10.1121/1.4944759>

de Groot-Hedlin, C. D. (2017). Infrasound propagation in tropospheric ducts and acoustic shadow zones. *Journal of the Acoustical Society of America*, *142*(4), 1816–1827. <https://doi.org/10.1121/1.5005889>

Delle Donne, D., Ripepe, M., Lacanna, G., Tamburello, G., Bitetto, M., & Aiuppa, A. (2016). Gas mass derived by infrasound and UV cameras: Implications for mass flow rate. *Journal of Volcanology and Geothermal Research*, *325*, 169–178. <https://doi.org/10.1016/j.jvolgeores.2016.06.015>

Embleton, T. F. W., Piercy, J. E., & Olson, N. (1976). Outdoor sound propagation over ground of finite impedance. *The Journal of the Acoustical Society of America*, *59*(2), 267–277. <https://doi.org/10.1121/1.380882>

Falco, L. E., Atchley, A. A., Gee, K. L., & Sparrow, V. W. (2006). Investigation of a single-point nonlinearity indicator in one-dimensional propagation. *AIP Conference Proceedings*, *838*(2006), 572–575. <https://doi.org/10.1063/1.2210421>

Fee, D., & Garces, M. (2007). Infrasonic tremor in the diffraction zone. *Geophysical Research Letters*, *34*, 1–5. <https://doi.org/10.1029/2007GL030616>

Fee, D., Izbekov, P., Kim, K., Yokoo, A., Lopez, T., Prata, F., et al. (2017). Eruption mass estimation using infrasound waveform inversion and ash and gas measurements: Evaluation at Sakurajima Volcano, Japan. *Earth and Planetary Science Letters*, *480*, 42–52. <https://doi.org/10.1016/j.epsl.2017.09.043>

Fee, D., & Matoza, R. S. (2013). An overview of volcano infrasound: From Hawaiian to Plinian, local to global. *Journal of Volcanology and Geothermal Research*, *249*, 123–139. <https://doi.org/10.1016/j.jvolgeores.2012.09.002>

Fee, D., Matoza, R. S., Gee, K. L., Neilsen, T. B., & Ogden, D. E. (2013). Infrasonic crackle and supersonic jet noise from the eruption of Nabro. *Geophysical Research Letters*, *40*, 4199–4203. <https://doi.org/10.1002/grl.50827>

Fee, D., McNutt, S. R., Lopez, T. M., Arnoult, K. M., Szuberla, C. A., & Olson, J. V. (2013). Combining local and remote infrasound recordings from the 2009 Redoubt Volcano eruption. *Journal of Volcanology and Geothermal Research*, *259*, 100–114. <https://doi.org/10.1016/j.jvolgeores.2011.09.012>

Fee, D., Yokoo, A., & Johnson, J. B. (2014). Introduction to an open community infrasound dataset from the actively erupting Sakurajima Volcano, Japan. *Seismological Research Letters*, *85*(6), 1151–1162. <https://doi.org/10.1785/0220140051>

Firstov, P. P., & Kravchenko, N. M. (1996). Estimation of the amount of explosive gas released in volcanic eruptions using air waves. *Volcanology and Seismology*, *17*(4–5), 547–560.

Gagnon, D. E. (2011). Bispectral analysis of nonlinear acoustic propagation (Unpublished doctoral dissertation), University of Texas at Austin.

Garcés, M., Fee, D., & Matoza, R. (2013). Volcano acoustics. In S. Fagents, T. Gregg, & R. Lopes (Eds.), *Modeling volcanic processes: The physics and mathematics of volcanism* (pp. 359–383). Cambridge: Cambridge University Press. <https://doi.org/10.1017/CBO9781139021562.016>

Garces, M. A. (2000). Theory of acoustic propagation in a multi-phase stratified liquid flowing within an elastic-walled conduit of varying cross-sectional area. *Journal of Volcanology and Geothermal Research*, *101*(1–2), 1–17. [https://doi.org/10.1016/S0377-0273\(00\)00155-4](https://doi.org/10.1016/S0377-0273(00)00155-4)

- Gee, K., Atchley, A., Falco, L., Shepherd, M., Ukeiley, L., Jansen, B., & Seiner, J. (2010). Bicoherence analysis of model-scale jet noise. *Journal of the Acoustical Society of America*, *128*(5), 211–216. <https://doi.org/10.1121/1.3484492>
- Gee, K. L., Gabrielson, T. B., Atchley, A. A., & Sparrow, V. W. (2005). Preliminary analysis of nonlinearity in military jet aircraft noise propagation. *AIAA Journal*, *43*(6), 1398–1401. <https://doi.org/10.2514/1.10155>
- Gee, K. L., Neilsen, T. B., & Atchley, A. A. (2013). Skewness and shock formation in laboratory-scale supersonic jet data. *The Journal of the Acoustical Society of America*, *133*(6), EL491–EL497. <https://doi.org/10.1121/1.4807307>
- Gee, K. L., Shepherd, M. R., Falco, L. E., Atchley, A. A., Ukeiley, L. S., Jansen, B. J., & Seiner, J. M. (2007). Identification of nonlinear and near-field effects in jet noise using nonlinearity indicators. In *Aiaa/ceas aeroacoustics conference* (Vol. 13, pp. 1–15). Rome, Italy. <https://doi.org/doi:10.2514/6.2007-3653>
- Gee, K. L., Sparrow, V. W., Atchley, A., & Gabrielson, T. B. (2007). On the perception of crackle in high-amplitude jet noise. *AIAA Journal*, *45*(3), 593–598. <https://doi.org/10.2514/1.26484>
- Gee, K. L., Sparrow, V. W., James, M. M., Downing, J. M., Hobbs, C. M., Gabrielson, T. B., & Atchley, A. A. (2008). The role of nonlinear effects in the propagation of noise from high-power jet aircraft. *The Journal of the Acoustical Society of America*, *123*(6), 4082–4093. <https://doi.org/10.1121/1.2903871>
- Genco, R., Ripepe, M., Marchetti, E., Bonadonna, C., & Biass, S. (2014). Acoustic wavefield and Mach wave radiation of flashing arcs in Strombolian explosion measured by image luminance. *Geophysical Research Letters*, *41*, 7135–7142. <https://doi.org/10.1002/2014GL061597>
- Green, D. N., Matoza, R. S., Vergoz, J., & Le Pichon, A. (2012). Infrasonic propagation from the 2010 Eyjafjallajkull eruption: Investigating the influence of stratospheric solar tides. *Journal of Geophysical Research*, *117*(21), 1–19. <https://doi.org/10.1029/2012JD017988>
- Hamilton, M. F., & Blackstock, D. T. (Eds.) (2008). *Nonlinear acoustics*. Melville, NY: Academic Press.
- Hamilton, M. F., & Morfey, C. L. (2008). Model Equations, *Nonlinear acoustics* (Chap. 3, pp. 41–63). Melville, NY: Academic Press.
- Iguchi, M. (2013). Magma Movement from the Deep to Shallow Sakurajima Volcano as Revealed by Geophysical Observations (Sakurajima Special Issue). *Bulletin of the Volcanological Society of Japan*, *58*(1), 1–18. https://doi.org/10.18940/kazan.58.1_1
- Iguchi, M., Tanegyri, T., Ohta, Y., Ueki, S., & Nakao, S. (2013). Characteristics of Volcanic Activity at Sakurajima Volcano's Showa Crater During the Period 2006 to 2011. *Bulletin of the Volcanological Society of Japan*, *58*(1), 115–135. <https://doi.org/10.18940/kazan.58.1115>
- Iguchi, M., Yakiwara, H., Tameguri, T., Hendrasto, M., & ichi Hirabayashi, J. (2008). Mechanism of explosive eruption revealed by geophysical observations at the Sakurajima, Suwanosejima and Semeru volcanoes. *Journal of Volcanology and Geothermal Research*, *178*(1), 1–9. <https://doi.org/10.1016/j.jvolgeores.2007.10.010>
- Ishihara, K. (1985). Dynamical analysis of volcanic explosion, *3*(3–4), 327–349. [https://doi.org/10.1016/0264-3707\(85\)90041-9](https://doi.org/10.1016/0264-3707(85)90041-9)
- Johnson, J. (2019). Local Volcano Infrasonic Monitoring, (Second). *Infrasound Monitoring for Atmospheric Studies* (pp. 989–1022). Cham, Switzerland: Springer International Publishing. <https://doi.org/10.1007/978-3-319-75140-5>
- Johnson, J. B., & Miller, A. J. C. (2014). Application of the monopole source to quantify explosive flux during vulcanian explosions at Sakurajima Volcano (Japan). *Seismological Research Letters*, *85*(6), 1163–1176. <https://doi.org/10.1785/0220140058>
- Johnson, J. B., & Ripepe, M. (2011). Volcano infrasonic: A review. *Journal of Volcanology and Geothermal Research*, *206*(3–4), 61–69. <https://doi.org/10.1016/j.jvolgeores.2011.06.006>
- Johnson, J. B., Ruiz, M. C., Ortiz, H. D., Watson, L. M., Viracucha, G., Ramon, P., & Almeida, M. (2018). Infrasonic Tornillos produced by Volcán Cotopaxi's Deep Crater. *Geophysical Research Letters*, *45*, 5436–5444. <https://doi.org/10.1029/2018GL077766>
- Johnson, J. B., Watson, L. M., Palma, J. L., Dunham, E. M., & Anderson, J. F. (2018). Forecasting the eruption of an open-vent volcano using resonant infrasonic tones. *Geophysical Research Letters*, *45*, 2213–2220. <https://doi.org/10.1002/2017GL076506>
- Jolly, A. D., Matoza, R. S., Fee, D., Kennedy, B. M., Iezzi, A. M., Fitzgerald, R. H., et al. (2017). Capturing the acoustic radiation pattern of Strombolian eruptions using infrasonic sensors aboard a tethered Aerostat, Yasur Volcano, Vanuatu. *Geophysical Research Letters*, *44*, 9672–9680. <https://doi.org/10.1002/2017GL074971>
- Jones, M. R., Riley, J., & Georges, T. (1986). *HARPA: A versatile three-dimensional Hamiltonian ray-tracing program for acoustic waves in the atmosphere above irregular terrain*. Boulder: U.S. Department of Commerce, National Oceanic and Atmospheric Administration.
- Kim, K., Fee, D., Yokoo, A., & Lees, J. M. (2015). Acoustic source inversion to estimate volume flux from volcanic explosions. *Geophysical Research Letters*, *42*, 5243–5249. <https://doi.org/10.1002/2015GL064466>
- Kim, K., & Lees, J. M. (2011). Finite-difference time-domain modeling of transient infrasonic wavefields excited by volcanic explosions. *Geophysical Research Letters*, *38*(6), 2–6. <https://doi.org/10.1029/2010GL046615>
- Kim, K., & Lees, J. M. (2014). Local volcano infrasonic and source localization investigated by 3D simulation. *Seismological Research Letters*, *85*(6), 1177–1186. <https://doi.org/10.1785/0220140029>
- Kim, K., Lees, J. M., & Ruiz, M. (2012). Acoustic multipole source model for volcanic explosions and inversion for source parameters. *Geophysical Journal International*, *191*, 1192–1204. <https://doi.org/10.1111/j.1365-246X.2012.05696.x>
- Kim, Y. C., & Powers, E. J. (1979). Digital bispectral analysis and its applications to nonlinear wave interactions. *IEEE Transactions on Plasma Science*, *7*(2), 120–131. <https://doi.org/10.1109/TPS.1979.4317207>
- Lacanna, G., Ichihara, M., Iwakuni, M., Takeo, M., Iguchi, M., & Ripepe, M. (2014). Influence of atmospheric structure and topography on infrasonic wave propagation. *Journal of Geophysical Research: Solid Earth*, *119*, 2988–3005. <https://doi.org/10.1002/2013JB010827>
- Lacanna, G., & Ripepe, M. (2013). Influence of near-source volcano topography on the acoustic wavefield and implication for source modeling. *Journal of Volcanology and Geothermal Research*, *250*, 9–18. <https://doi.org/10.1016/j.jvolgeores.2012.10.005>
- Lamb, O. D., De Angelis, S., & Lavallée, Y. (2015). Using infrasonic to constrain ash plume rise. *Journal of Applied Volcanology*, *4*, 20. <https://doi.org/10.1186/s13617-015-0038-6>
- Lonzaga, J. B., Waxler, R. M., Assink, J. D., & Talmadge, C. L. (2015). Modelling waveforms of infrasonic arrivals from impulsive sources using weakly non-linear ray theory. *Geophysical Journal International*, *200*, 1347–1361. <https://doi.org/10.1093/gji/ggu479>
- Marchetti, E., Ripepe, M., Delle Donne, D., Genco, R., Finizola, A., & Garaebiti, E. (2013). Blast waves from violent explosive activity at Yasur Volcano, Vanuatu. *Geophysical Research Letters*, *40*, 5838–5843. <https://doi.org/10.1002/2013GL057900>
- Matoza, R. S., Fee, D., Garcés, M. A., Seiner, J. M., Ramón, P. A., & Hedlin, M. A. H. (2009). Infrasonic jet noise from volcanic eruptions. *Geophysical Research Letters*, *36*, 2–6. <https://doi.org/10.1029/2008GL036486>
- Matoza, R. S., Fee, D., Green, D. N., Le Pichon, A., Vergoz, J., Haney, M. M., & Ceranna, L. (2018). Local, regional, and remote seismo-acoustic observations of the April 2015 VEI 4 eruption of Calbuco Volcano, Chile. *Journal of Geophysical Research: Solid Earth*, *123*, 3814–3827. <https://doi.org/10.1002/2017JB015182>
- Matoza, R., Fee, D., Green, D., & Mialle, P. (2019). Volcano infrasonic and the International Monitoring System (Second). In A. Le Pichon (Ed.), *Infrasound monitoring for atmospheric studies* (pp. 1023–1077). Cham: Springer International Publishing. <https://doi.org/10.1007/978-3-319-75140-5>

- Matoza, R. S., Fee, D., & Lopez, T. M. (2014). Acoustic characterization of explosion complexity at Sakurajima, Karymsky, and Tungurahua Volcanoes. *Seismological Research Letters*, 85(6), 1187–1199. <https://doi.org/10.1785/0220140110>
- Matoza, R. S., Fee, D., Neilsen, T. B., Gee, K. L., & Ogdén, D. E. (2013). Aeroacoustics of volcanic jets: Acoustic power estimation and jet velocity dependence. *Journal of Geophysical Research: Solid Earth*, 118, 6269–6284. <https://doi.org/10.1002/2013JB010303>
- Matoza, R. S., Garces, M. A., Chouet, B. A., D'Auria, L., Hedlin, M. A., De Groot-Hedlin, C., & Waite, G. P. (2009). The source of infrasound associated with long-period events at Mount St. Helens. *Journal of Geophysical Research*, 114, 1–38. <https://doi.org/10.1029/2008JB006128>
- Matoza, R. S., Green, D. N., Le Pichon, A., Shearer, P. M., Fee, D., Mialle, P., & Ceranna, L. (2017). Automated detection and cataloging of global explosive volcanism using the International Monitoring System infrasound network. *Journal of Geophysical Research: Solid Earth*, 122, 2946–2971. <https://doi.org/10.1002/2016JB013356>
- Matoza, R. S., Le Pichon, A., Vergoz, J., Herry, P., Lalande, J. M., Lee, H. I., et al. (2011). Infrasonic observations of the June 2009 Sarychev Peak eruption, Kuril Islands: Implications for infrasonic monitoring of remote explosive volcanism. *Journal of Volcanology and Geothermal Research*, 200(1-2), 35–48. <https://doi.org/10.1016/j.jvolgeores.2010.11.022>
- McKee, K., Fee, D., Yokoo, A., Matoza, R. S., & Kim, K. (2016). Analysis of gas jetting and fumarole acoustics at Aso Volcano, Japan. *Journal of Volcanology and Geothermal Research*, 340, 16–29. <https://doi.org/10.1016/j.jvolgeores.2017.03.029>
- Medici, E. F., Allen, J. S., & Waite, G. P. (2013). Modeling shock waves generated by explosive volcanic eruptions. *Geophysical Research Letters*, 41, 414–421. <https://doi.org/10.1002/2013GL058340>
- Miller, K. G., & Gee, K. L. (2018). Model-scale jet noise analysis with a single-point, frequency-domain nonlinearity indicator. *The Journal of the Acoustical Society of America*, 143(6), 3479–3492. <https://doi.org/10.1121/1.5041741>
- Miller, K. G., Gee, K. L., & Reichman, B. O. (2016). Asymptotic behavior of a frequency-domain nonlinearity indicator for solutions to the generalized Burgers equation. *The Journal of the Acoustical Society of America*, 140(6), 522–527. <https://doi.org/10.1121/1.4971880>
- Miwa, T., & Toramaru, A. (2013). Conduit process in vulcanian eruptions at Sakurajima volcano, Japan: Inference from comparison of volcanic ash with pressure wave and seismic data. *Bulletin of Volcanology*, 75(685), 1–13. <https://doi.org/10.1007/s00445-012-0685-y>
- Morfeý, C. L., & Howell, G. P. (1981). Nonlinear propagation of aircraft noise in the atmosphere. *AIAA Journal*, 19(8), 986–992. <https://doi.org/10.2514/3.51026>
- Morrissey, M. M., & Chouet, B. A. (1997). Burst conditions of explosive volcanic eruptions recorded on microbarographs. *Science*, 275(1997), 1290–1293. <https://doi.org/10.1126/science.275.5304.1290>
- Muhlestein, M. B., Gee, K. L., Thomas, D. C., & Neilsen, T. B. (2012). Prediction of nonlinear propagation of noise from a solid rocket motor. *Proceedings of Meetings on Acoustics*, 18, 040006. <https://doi.org/10.1121/1.4755357>
- Muramatsu, D., Aizawa, K., Yokoo, A., Iguchi, M., & Tameguri, T. (2018). Estimation of vent radii from video recordings and infrasound data analysis: Implications for volcanic eruptions from Sakurajima Volcano, Japan. *Geophysical Research Letters*, 45, 12,829–12,836. <https://doi.org/10.1029/2018gl079898>
- Petitjean, B. P., Viswanathan, K., & McLaughlin, D. K. (2006). Acoustic pressure waveforms measured in high speed jet noise experiencing nonlinear propagation. *International Journal of Aeroacoustics*, 5(2), 193–215. <https://doi.org/10.1260/14754720677629835>
- Pierce, A. D. (1981). *Acoustics: An introduction to its physical principles and applications*. New York, New York: McGraw-Hill.
- Piercy, J. E., Embleton, T. F. W., & Sutherland, L. C. (1977). Review of noise propagation in the atmosphere. *The Journal of the Acoustical Society of America*, 61(6), 1403–1418. <https://doi.org/10.1121/1.381455>
- Reichman, B. O., Gee, K. L., Neilsen, T. B., & Miller, K. G. (2016). Quantitative analysis of a frequency-domain nonlinearity indicator. *The Journal of the Acoustical Society of America*, 139(5), 2505–2513. <https://doi.org/10.1121/1.4945787>
- Riedel, K., & Sidorenko, A. (1995). Minimum bias multiple taper spectral estimation. *IEEE Transactions on Signal Processing*, 43(1), 188–195.
- Ripepe, M., Bonadonna, C., Folch, A., Delle Donne, D., Lacanna, G., Marchetti, E., & Höskuldsson, A. (2013). Ash-plume dynamics and eruption source parameters by infrasound and thermal imagery: The 2010 Eyjafjallajökull eruption. *Earth and Planetary Science Letters*, 366, 112–121. <https://doi.org/10.1016/j.epsl.2013.02.005>
- Sutherland, L. C., & Bass, H. E. (2004). Atmospheric absorption in the atmosphere up to 160 km. *The Journal of the Acoustical Society of America*, 115(3), 1012–1032. <https://doi.org/10.1121/1.1631937>
- Taddeucci, J., Sesterhenn, J., Scarlato, P., Stampka, K., Del Bello, E., Pena Fernandez, J., & Gaudin, J. (2014). High-speed imaging, acoustic features, and aeroacoustic computations of jet noise from Strombolian (and Vulcanian) explosions. *Geophysical Research Letters*, 41, 3096–3102. <https://doi.org/10.1002/2014GL059925>
- Taflove, A., & Hagness, S. C. (2005). *Computational electrodynamics: The finite-difference time-domain method* (3rd ed.). Norwood, MA: Artech House.
- Tameguri, T., Iguchi, M., & Ishihara, K. (2002). Mechanism of explosive eruptions from moment tensor analyses of explosion earthquakes at Sakurajima Volcano, Japan. *Bulletin of the Volcanological Society of Japan*, 47(4), 197–215. https://doi.org/10.18940/kazan.47.4_197
- Uhira, K., & Takeo, M. (1994). The source of explosive eruptions of Sakurajima volcano, Japan. *Journal of Geophysical Research*, 99, 17,775–17,789. <https://doi.org/10.1029/94JB00990>
- Watson, L. M., Dunham, E. M., & Johnson, J. B. (2019). Simulation and inversion of harmonic infrasound from open-vent volcanoes using an efficient quasi-1D crater model. *Journal of Volcanology and Geothermal Research*, 380, 64–79. <https://doi.org/10.1016/j.jvolgeores.2019.05.007>
- Waxler, R., & Assink, J. (2019). Propagation modeling through realistic atmosphere and benchmarking. In A. L. Pichon, E. Blanc, & A. Hauchecorne (Eds.), *Infrasound monitoring for atmospheric studies* (pp. 509–549). Cham: Springer. <https://doi.org/10.1007/978-1-4020-9508-5>
- Whitaker, R. W., & Norris, D. E. (2008). Infrasound propagation. In D. Havelock, S. Kuwano, & M. Vorlander (Eds.), *Handbook of signal processing in acoustics* pp. 1497–1519. New York, New York: Springer. https://doi.org/10.1007/978-0-387-30441-0_82
- Woulff, G., & McGetchin, T. R. (1976). Acoustic noise from volcanoes—Theory and experiment. *Geophysical Journal of the Royal Astronomical Society*, 45(3), 601–616. <https://doi.org/10.1111/j.1365-246X.1958.tb05346.x>
- Yamada, T., Aoyama, H., Nishimura, T., Iguchi, M., & Hendrasto, M. (2017). Volcanic eruption volume flux estimations from very long period infrasound signals. *Geophysical Research Letters*, 44, 143–151. <https://doi.org/10.1002/2016GL071047>
- Yokoo, A., Iguchi, M., Tameguri, T., & Yamamoto, K. (2013). Processes prior to outbursts of vulcanian eruption at Showa Crater of Sakurajima Volcano. *Bulletin of the Volcanological Society of Japan*, 58(1), 163–181. https://doi.org/10.18940/kazan.58.1_163
- Yokoo, A., & Ishihara, K. (2007). Analysis of pressure waves observed in Sakurajima eruption movies. *Earth, Planets and Space*, 59(3), 177–181. <https://doi.org/10.1186/BF03352691>
- Yokoo, A., Suzuki, Y. J., & Iguchi, M. (2014). Dual infrasound sources from a vulcanian eruption of Sakurajima Volcano inferred from cross-array observation. *Seismological Research Letters*, 85(6), 1212–1222. <https://doi.org/10.1785/0220140047>

Yokoo, A., Tameguri, T., & Iguchi, M. (2009). Swelling of a lava plug associated with a Vulcanian eruption at Sakurajima Volcano, Japan, as revealed by infrasound record: Case study of the eruption on January 2, 2007. *Bulletin of Volcanology*, 71(6), 619–630. <https://doi.org/10.1007/s00445-008-0247-5>